2014-12-01

Modeling and Testing of Bistable Waterbomb Base Configurations

Brandon Holbrook Hanna
Brigham Young University - Provo

Modeling and Testing of Bistable Waterbomb Base Configurations

Brandon H. Hanna

A thesis submitted to the faculty of
Brigham Young University
in partial fulfillment of the requirements for the degree of

Master of Science

Larry L. Howell, Chair
Spencer P. Magleby
Brian D. Jensen

Department of Mechanical Engineering

Brigham Young University

December 2014

ABSTRACT

Modeling and Testing of Bistable Waterbomb Base Configurations

Brandon H. Hanna
Department of Mechanical Engineering, BYU
Master of Science

Origami is making an impact in engineering as solutions to problems are being found by applying origami principles (eg. flat-foldability) and using specific crease patterns as inspiration. This thesis presents an in-depth analysis of a particular origami fold – the waterbomb base – to facilitate its use in future engineering problems. The watebomb base is of interest due to its familiarity to the origami community, simple topology (can be made by folding a single sheet of paper four times), scalability, generalizability, and interesting kinetic behavior. It can behave as a nonlinear spring as well as a one- or two-way bistable mechanism. This thesis presents models of the kinetic behavior of the traditional waterbomb base as well as some non-traditional variants to be used as tools in future development of waterbomb-base-inspired mechanisms. In all cases considered here, developability as well as rotational symmetry in both the geometry and motion of the mechanisms are assumed.

The thesis provides an introduction to origami and reviews some of the ways in which it has been studied and applied in engineering fields. The waterbomb base is also presented as a specific origami fold with practical application potential.

Models for the behavior of the traditional waterbomb base are introduced and its potential usefulness as a testbed for actuation methods is discussed. Models are developed for its kinematic and bistable behavior, including the forces needed to transition between stable states. These models are validated by comparison to physical prototype testing and finite element analysis.

The thesis introduces the generalized waterbomb base (WB) and generalized split-fold waterbomb base (SFWB). The WB maintains the pattern of alternating mountain and valley folds around the vertex but in this generalized case any even number of folds greater than or equal to 6 is allowed. An SFWB is created by splitting each fold of a WB into two "half folds", effectively doubling the number of folds and links but halving the deflection at each fold. The same models that were developed for the traditional waterbomb base are developed for the WB and the SFWB and a few potential applications are discussed.

Keywords: origami-based mechanism, waterbomb base, bistable mechanism, smart material test bed

ACKNOWLEDGMENTS

I must first thank my wife, Natalie, for being patient and supportive while I was working on this thesis. This wouldn't have happened without you. Thanks also to Clark for helping us have fun amidst the madness that is life from time to time, and my parents for their love and support.

I am also profoundly grateful for the positive and supportive research environment I have been a part of. The CMR has been a great place to discuss ideas and solve problems, and I will miss everyone there.

A special thanks goes to Dr. Howell, my advisor, for helping me to keep moving forward when we ran into challenges and results we weren't expecting, and for his experienced perspective that helped me to maintain my excitement for this work.

Chapter 2 has been published as "Waterbomb Base: A Symmetric Single-Vertex Bistable Origami Mechanism" in the journal Smart Materials and Structures with Jason M. Lund, Robert J. Lang, Spencer P. Magleby, and Larry L. Howell as co-authors. Chapter 3 has been submitted for publication as "Force-deflection modeling for generalized origami waterbomb-base mechanisms" with Spencer P. Magleby, Robert J. Lang, and Larry L. Howell as co-authors.

This material is based on work supported by the National Science Foundation and the Air Force Office of Scientific Research under NSF Grant EFRI-ODISSEI-1240417.

TABLE OF CONTENTS

LIST OF TABLES

LIST OF FIGURES

CHAPTER 1. INTRODUCTION

1.1 Background

Origami has been practiced as an art form for hundreds of years. Recently, however, it has been gaining attention for its potential to provide novel solutions to practical problems. Some studies have focused on understanding the kinematics of origami folding for application in robotics and the packaging industry [1, 2]. Greater understanding of folding methods has also led to the development of origami-based folding algorithms that have been used to address complex challenges such as how to best fold automotive airbags [3].

In attempting to understand origami for use in design, one useful method of modeling these mechanisms is to approximate the facets as rigid links and the folds as revolute joints [4]. However, folded materials behave differently than traditional joints and this must be accounted for. Several studies have investigated the behavior of creased and folded materials [5–7], and these results can be used if they include the materials of interest. A more general approach that is not restricted to a small number of materials is to consider origami structures as compliant mechanisms. A compliant mechanism's motion is accomplished at least in part by the deflection of flexible members rather than by the rotation or translation of traditional joints [8]. Because origami mechanisms rely on folded and deflected paper rather than hinges or other joints for their motion, they are compliant mechanisms and can be modeled as such [9].

By combining these various approaches, origami-based design has directly influenced the development of collapsible kayaks [10], foldable dinnerware [11], space telescope lenses [12] and deployable solar arrays [13], shock-absorbing automotive crash boxes [14], soft robotic actuators [15], self-folding robots [16], and reprogrammable metamaterials [17]. These examples show that origami has the potential to inspire solutions to a wide range

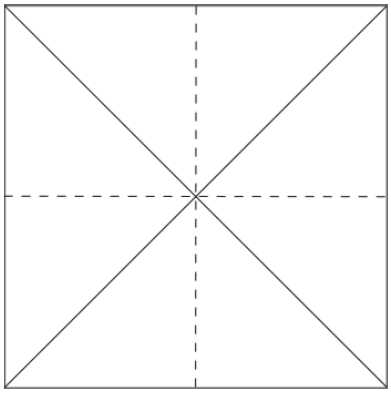

Figure 1.1: Waterbomb base fold pattern. Solid lines indicate mountain folds (facets point upward at the fold) and dashed lines indicate valley folds (facets point downward at the fold).

of problems, and this potential will expand as origami principles and designs are better understood.

One origami design of interest is the waterbomb base. Although the name waterbomb base has only been applied to it relatively recently [18], this origami mechanism has been in use for centuries [19] and it is one of several basic starting points for more complex origami designs. It is made from a square paper with only 4 folds, as shown in Figure 1.1.

The waterbomb base exhibits bistable behavior, as shown in Figure 1.2. When it is initially folded it rests in its first stable position. If the vertex is deflected toward a plane and released, it will return to its initial position. However, if the vertex is deflected past the plane and released it will move into its second stable position. It is particularly interesting to note that the mountain folds remain mountain folds in both positions and the valley folds remain valley folds. This unique behavior has potential utility in a variety of engineering systems and situations, such as a testbed for smart materials actuation [20].

1.2 Research objectives

The goal of this research is to develop a greater understanding of the behavior of the waterbomb base and demonstrate its application to engineering and product design problems. The focus is on how this base can be modified, adapted and controlled.

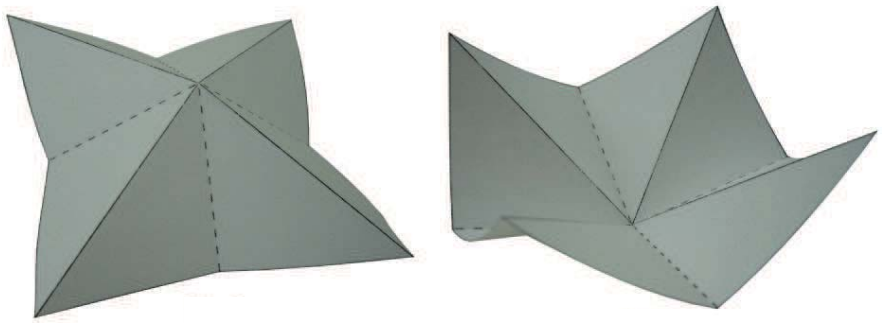

(a) (b)

Figure 1.2: Waterbomb base bistable positions (a) 1 and (b) 2. Notice that mountain folds remain mountain folds in both positions, and the same is true for valley folds.

The thesis research accomplished the following objectives:

- Develop kinematic relationships to define the waterbomb base in any state.
- Develop the means to predict and control bistable behavior of the waterbomb base.
- Validate mathematical models and derived relationships by testing physical prototypes.
- Explore variations and combinations of the waterbomb base.
- Identify potential applications for the waterbomb base.

1.3 Approach

A kinematic analysis of the waterbomb base is completed to define its position in any state. This analysis is carried out using spherical kinematics.

A potential energy analysis is then completed to enable the prediction of where stable states occur and how much energy is required to move between them. In this analysis the facets are treated as rigid panels and the folds as small length-flexural pivots, utilizing the methods of compliant mechanisms to model the energetic behavior of the mechanism. Figure 1.3 is a sample potential energy plot from preliminary work with the waterbomb base.

Force-deflection behavior is also modeled by using the principle of virtual work in conjunction with the previous analyses.

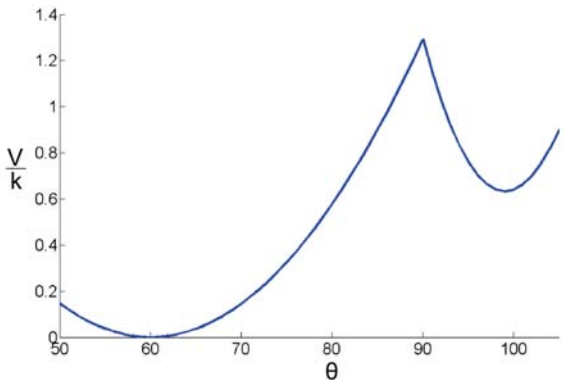

Figure 1.3: Potential energy plot from initial attempts to analyze the waterbomb base. V/k is the nondimensionalized potential energy and θ is the input from which the position of the waterbomb base is determined.

Position, potential energy, and force-deflection analyses are validated by comparisons with 3-D CAD models, finite element analysis, and physical prototype tests. Prototypes are produced by a combination of machining and laser cutting. Testing of prototypes is done with an Instron tensile testing machine.

With this understanding of waterbomb base behavior in hand, variations and permutations of the waterbomb base are explored to see how it can be modified to accomplish different tasks. The location, orientation, and number of folds are changed and the effects on bistable behavior and general motion are studied, and a few potential applications are discussed.

CHAPTER 2. WATERBOMB BASE: A SYMMETRIC SINGLE-VERTEX BISTABLE ORIGAMI MECHANISM

2.1 Introduction

The purpose of this chapter is to develop a quantitative understanding of the origami waterbomb base's kinematic and bistable behavior to facilitate its use as a test bed for smart material development and to enable its application to engineering and product design. The origami waterbomb base is a fundamental origami fold that serves as a foundation for more complex origami models [21]. The waterbomb base crease pattern is shown in Figure 2.1, and folded versions are shown in Figure 2.2. It has spring-like and bistable properties that may be considered for use outside of artistic origami, including use in materials other than paper. The waterbomb base shows promise as a test bed for programmable materials and embedded actuators. Test beds can be an effective way to evaluate, validate, and refine actuation approaches. For example, a flat pattern that folds itself into a box is a common test bed that has been used to investigate smart materials and actuators involving thermally sensitive hydrogels [22], pre-strained polymers [23], magneto active elastomers (MAE) [24], and foldable PCB arrays [25], to name a few examples. The waterbomb base has properties that make it well suited for such a test bed. Some of these properties are shared with other crease patterns, but the combination of properties makes it particularly useful. Several of these are described below:

1. The topology is straightforward, which has the following advantages as a test bed:
   (a) *Manufacturable.* It is easily manufactured.
   (b) *Transferable.* The design (crease pattern) is transferable, enabling sharing between labs across the world.

(c) *Scalable.* It is scalable across a wide range of size domains for use with actuators of different sizes and classes.

(d) *Named.* The fold pattern is commonly recognized by the name waterbomb base and therefore is easily communicated.

2. The fold pattern is attractive from an engineering analysis and application perspective due to the following properties:

   (a) *Rigid foldable.* This pattern is comprised of rigid facets and all motion occurs at the joints between facets, simplifying the kinematic and energy analyses compared to patterns in which facets must deflect.

   (b) *Generalized and expanded for different designs.* Variations of the waterbomb base can be made with 6, 10, or any even number of folds greater than 2 to accomodate different designs.

3. There are different phases of motion, each with different levels of actuation complexity, making it appropriate for a wide range of tests for different classes of actuators. The three primary phases of actuated motions are listed below:

   (a) *Nonlinear spring actuation.* Its force-deflection curve is nonlinear but unimodal when its motion is between the first stable equilibrium position and the unstable equilibrium position.

   (b) *One-way bistable actuation.* With a sufficiently large input displacement, the device transitions from the first stable equilibrium position, through the unstable equilibrium position, to the second stable equilibrium position.

   (c) *Reversible bistable actuation.* In this case the device transitions from first to second stable equilibrium positions, but also from second to first stable equilibrium positions.

4. There are potential engineering applications of the waterbomb base (e.g. reconfigurable surfaces, two-state membranes, switches), and successfully introducing integrated ac-

tuation methods to the waterbomb base has the potential for direct application. It is hoped that this work will facilitate the development of these applications.

An understanding of the waterbomb base motion, force-deflection relationship, and bistable behavior will enable its use as a test bed and facilitate its use in engineering application.

Although this is the first detailed exploration of the waterbomb base from an engineering perspective, many other origami structures and methods have been studied previously. The kinematics of general origami folding have been investigated [1, 2] and folding algorithms have been developed and applied to complex problems such as automotive airbag folding [3] and deployable solar panels [13]. Complete origami structures have been modeled by approximating folds as hinges and facets as rigid links [4]. By combining many of these concepts, origami-inspired solutions have already been found for a variety of problems. For example, the foldable/deployable nature of many origami structures are attractive in settings where mechanisms must be small during transport and deploy to full size for use and have already found use in the design of collapsible kayaks [10], foldable dinnerware [11], and space telescope lenses [12]. Collapsing folds have also been used in the design of shock-absorbing automotive crash boxes [26] and soft robotic actuators [15].

Several different approaches have been used to understand and model the behavior of the folds themselves. Direct investigation of the mechanical response of creased and folded paper materials undergoing deflection has found that these materials tend to display nonlinear bending stiffness [5, 6, 27, 28]. Work has also been done to understand how the crease behavior of other materials compares to that of paper [7]. The results of these studies could be used to develop bending stiffnesses to use in modeling the waterbomb base, but these functions would have to be reevaluated each time a new material is considered. A more general approach is to approximate the fold as a compliant joint so that the results are not restricted to a single material. A compliant mechanism is one in which motion is accomplished completely or in part by the deflection of flexible members rather than by traditional rotational or translational joints [8]. Since origami mechanisms do not make use of hinges or other traditional joints and instead rely on deflection of the paper for motion, they are compliant mechanisms and this method of modeling is appropriate [9].

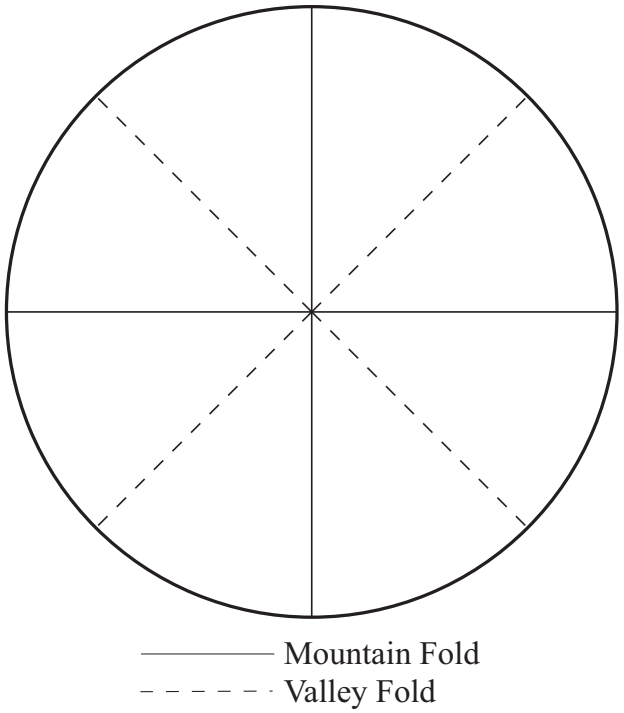

Figure 2.1: Waterbomb base crease pattern. The waterbomb base is usually folded from a square sheet of paper but a circular paper is used here so that all folds have the same length.

It is also worth noting that compliant mechanisms are well suited to bistable applications. Previous studies have considered the design and analysis of compliant bistable mechanisms [29–32], and the general principles of bistable mechanisms apply.

This chapter describes the waterbomb base's crease pattern and behavior. A kinematic analysis to define the waterbomb base in any state is completed followed by a potential energy analysis to understand and enable the prediction of bistable behavior. To validate these analyses, a physical prototype was constructed and tested. Finally, finite element and virtual work analyses based upon the prototype were completed to investigate force-deflection behavior.

2.2 Description

The crease pattern for a typical waterbomb base is shown in Figure 2.1. The solid circle represents the outside edge of the paper and the straight lines are fold lines with all

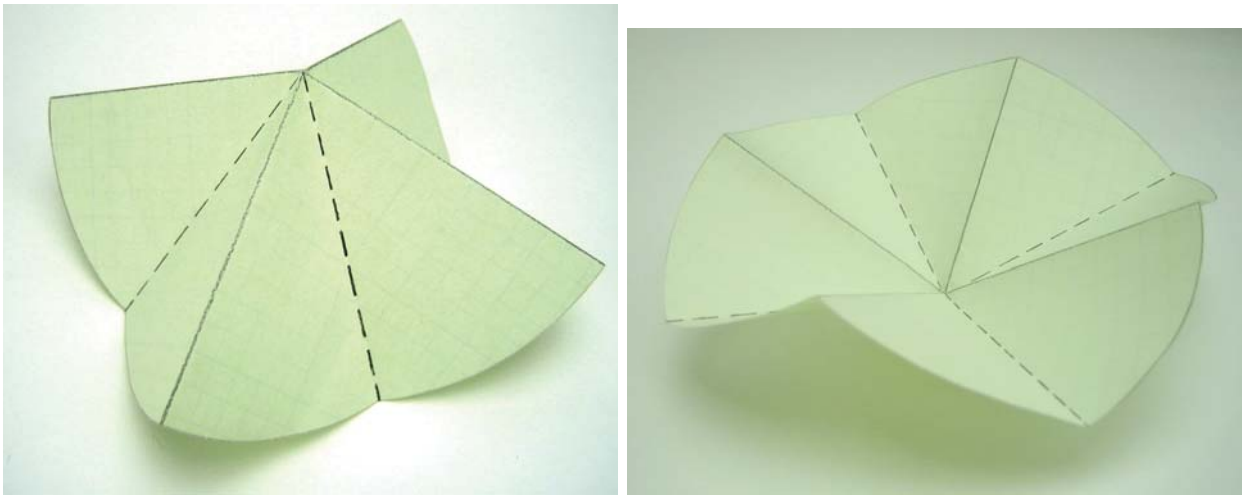

(a) (b)

Figure 2.2: Waterbomb base (a) first stable equilibrium position and (b) second stable equilibrium position. Mountain folds are indicated by solid lines and valley folds by dashed lines. Note that mountain folds remain mountain folds and valley folds remain valley folds in both positions.

neighboring pairs separated by 45°. A circular sheet of paper is shown here so that the folds all have the same length. Mountain folds (solid lines) are folded such that the two panels that meet at the fold point upward while valley folds (dashed lines) are folded so that the adjacent panels point downward, as shown in Figure 2.2.

The waterbomb base can be classified as a bistable mechanism because it has two stable equilibrium states. It moves to one of these two positions when no external loads are applied because the potential energy stored in the mechanism is at a local minimum at each of these points [8]. When moved away from one of these positions (to a higher energy state) and then released, it returns to the nearest stable position (the lower energy state). Bistable mechanisms also have an unstable equilibrium position where the mechanism can be in equilibrium but a small disturbance will cause it to leave this unstable position and move to one of its stable states. (A light switch is an example of a common bistable mechanism where its stable positions are the “on” and “off” positions.)

When a waterbomb base is folded it rests in one of two stable positions, as shown in Figure 2.2. Figure 2.2(a) shows the first stable position, in which the vertex (the point where all folds intersect) points up. If the vertex is displaced so that the structure flattens

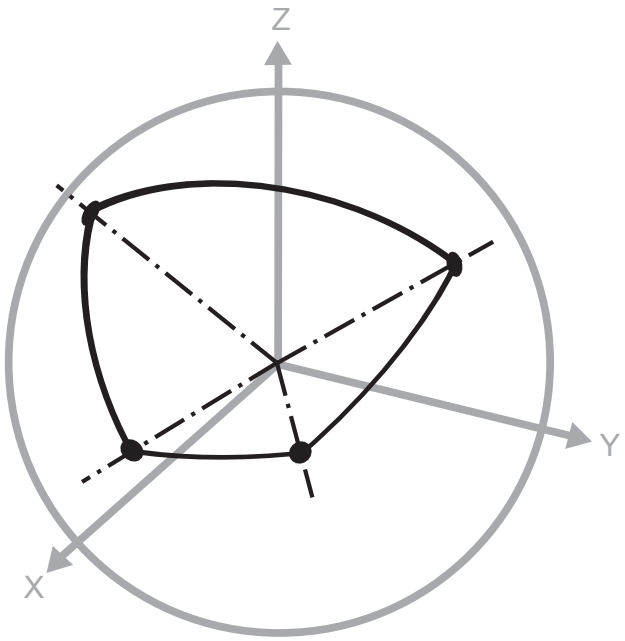

Figure 2.3: Schematic of a sample spherical mechanism. The links rest on the surface of the sphere and the axes of rotation intersect at the center of the sphere. The waterbomb base is a spherical mechanism with 8 links in which the vertex (where all of the folds meet) is at the center of the sphere.

out and approaches a plane, it will return to the original position when released. If, however, the vertex is displaced past the plane, it snaps through the unstable position and moves to the second stable position (Figure 2.2(b)). The second bistable position is also called a "preliminary fold" [21].

The waterbomb base also qualifies as a spherical mechanism. By definition, a spherical mechanism is one in which all axes of rotation intersect at a common point, as illustrated in Figure 2.3. Bistable spherical compliant mechanisms have been considered previously [33,34], but these mechanisms had fewer links than are found in a waterbomb base. Nevertheless, some of the concepts used in these investigations are applicable to the current study.

An interesting behavior in the waterbomb base is that the direction of each fold does not change throughout the bistable motion: the mountain folds remain mountain folds in both stable positions and the valley folds remain valley folds, as shown in Figure 2.2.

In order to simplify the following analyses it is assumed that the waterbomb base is symmetric. All sector angles (angles between neighboring folds) are the same, all mountain

folds have the same value at any instant, and the same is true for all valley folds. Symmetry of motion is also assumed such that when the waterbomb base is deflected, all mountain folds are deflected the same amount and at the same rate, and the same holds for all valley folds. The symmetry is maintained for all positions investigated.

We note in passing that non-symmetric configurations – where sector angles and/or the bias on dihedral angles vary – may also be considered, and that symmetric initial conditions may well give rise to non-symmetric equilibrium states (spontaneous symmetry-breaking). Analytical solutions to these non-symmetric configurations can be found but involve large numbers of variables and several layers of nested trigonometric functions making them less accessible for application compared to the special case. In-depth exploration of these solutions will be left for future studies.

2.3 Position analysis

The waterbomb base was modeled by treating the panels as rigid links and the folds as hinges. When symmetry is required and all folds are biased toward a set of initial angles, the waterbomb base reduces from multiple degrees of freedom to a one degree of freedom device and all link positions can be determined from a single input.

Because the waterbomb base can be classified as a spherical mechanism, the methods of spherical kinematics are applicable and Figures 2.4–2.6 show the notation used in this analysis. The input, θ, is the angle between a valley fold and the vertical axis, V, that passes through the vertex. γ_m is the angle of each mountain fold and γ_v is the angle of each valley fold (see Figure 2.4) where the fold angles are measured in terms of deviation from straightness. Therefore, a fold angle of 0° indicates a straight condition (flat, unfolded paper), valley folds are assigned positive values, and mountain folds are assigned negative values.

The relationships between θ, γ_m, and γ_v are different on each side of the unstable equilibrium position (θ=90°), therefore one set of expressions is derived for $0° \leq \theta \leq 90°$ (Range a) and another set for $90° \leq \theta \leq 135°$ (Range b). Note that θ has fewer possible values in Range b than in Range a. This is because the two regimes of motion are non-symmetric and interference between facets occurs at a different point in each regime.

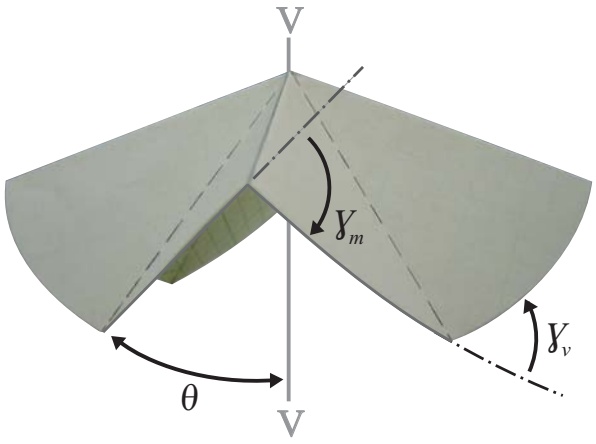

Figure 2.4: The input θ is the angle between any valley fold and the vertical axis V that runs through the vertex. γ_m is the angle of all mountain folds and γ_v is the angle of all valley folds.

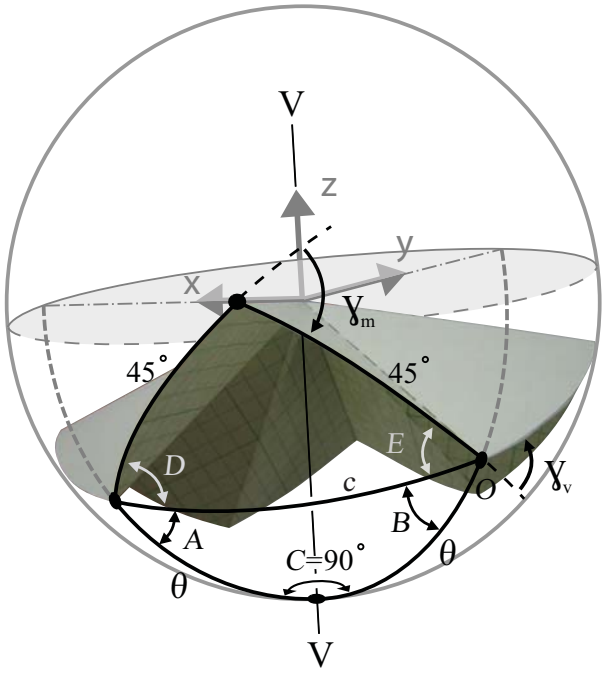

Figure 2.5: Spherical triangles used to compute γ_m and γ_v for $0°\leq\theta\leq90°$ (Range a).

2.3.1 $0°\leq\theta\leq90°$ (Range a)

The spherical triangles shown in Figure 2.5 were used to find the relationships between γ_m, γ_v, and θ. The radius of the sphere on which all of these triangles lie has been assigned

a value of 1. The 45° links and 90° angle are direct results of the geometry of the waterbomb base. Using the formulas for right and general spherical triangles [35] and applying A=B and D=E due to symmetry, three intermediate values are solved as

$$c = \cos^{-1}[\cos^2(\theta)] \tag{2.1}$$

$$B = \sin^{-1}\left[\frac{\sin(\theta)}{\sin(c)}\right] \tag{2.2}$$

$$E = \cos^{-1}\left[\frac{\sin(c)}{\cos(c)+1}\right] \tag{2.3}$$

where c is the hypotenuse of triangle ABC. Using these values, γ_m was determined using the cosine law for sides and γ_v by summing all of the angles about the point O:

$$\gamma_m = \cos^{-1}[2\cos(c)-1]-180^\circ \tag{2.4}$$

$$\gamma_{va} = 2(B+E-90^\circ) \tag{2.5}$$

where γ_{va} is the value of γ_v in Range a ($0^\circ \leq \theta \leq 90^\circ$). Substituting from equations (2.1)–(2.3) and simplifying produces

$$\gamma_m = \cos^{-1}[2\cos^2(\theta)-1]-180^\circ \tag{2.6}$$

$$\gamma_{va} = 2\left\{\sin^{-1}\left[\frac{\sin(\theta)}{\sin(c)}\right]+\cos^{-1}\left[\frac{\sin(c)}{\cos(c)+1}\right]-90^\circ\right\} \tag{2.7}$$

2.3.2 $90^\circ \leq \theta \leq 135^\circ$ (Range b)

Using the same methods described in the previous section but with the spherical triangles shown in Figure 2.6, c and γ_m are the same as defined in equations (2.1) and (2.6) but γ_v in Range b, γ_{vb}, is defined as

$$\gamma_{vb} = 2\left\{\cos^{-1}\left[\csc(c)-\cot(c)\right]-\sin^{-1}\left[\frac{\sin(\theta)}{\sin(c)}\right]+90^\circ\right\} \tag{2.8}$$

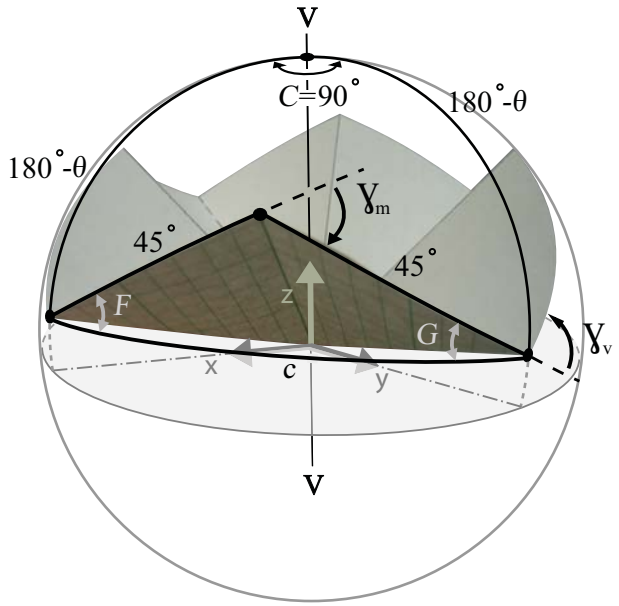

Figure 2.6: Spherical triangles used to compute γ_m and γ_v for $90°{\leq}\theta{\leq}135°$ (Range b).

Figure 2.7 shows a plot of γ_m versus γ_v. Each point on the plot corresponds to a unique value of θ between 0° and 135°. The unstable equilibrium position occurs when $\gamma_m{=}\gamma_v{=}0°$, which corresponds to $\theta{=}90°$. Also, the plot is symmetric about the line that passes through the points (-180,180) and (0,0). As an initial verification, a 3-D CAD model was constructed and several of its positions were compared against the results shown above.

2.4 Potential energy analysis

The waterbomb base potential energy analysis was carried out by modeling each fold as a compliant small-length flexural pivot with the parameters shown in Figure 2.8. The potential energy stored in a small-length flexural pivot [8], and therefore in each fold, is given by

$$V = \frac{1}{2}k(\Theta)^2 \tag{2.9}$$

where Θ is the rotational deflection away from the neutral position and the stiffness k is given as

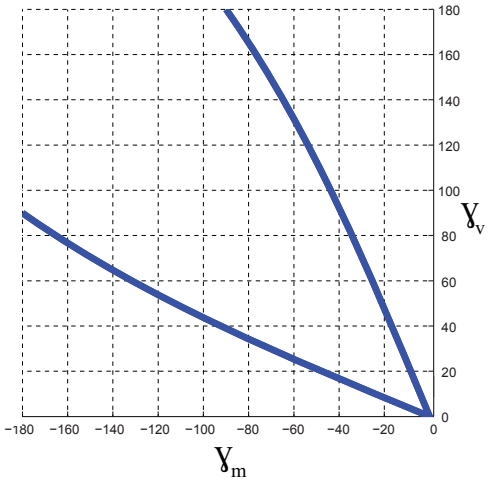

Figure 2.7: Plot of γ_m and γ_v angles. Each of these points is unique to a value of θ between 0° and 135°. The unstable equilibrium position occurs at the point where $\gamma_m = \gamma_v = 0°$ ($\theta = 90°$). The plot is symmetric about the line passing through the points (-180,180) and (0,0).

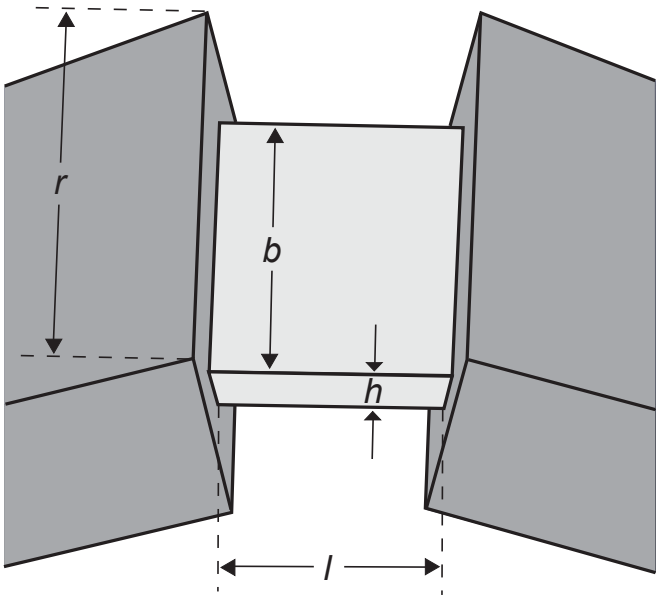

Figure 2.8: Parameters used to define small-length flexural pivots in the waterbomb base. The lighter color indicates the flexible-joint material and the darker color represents the rigid-link material.

$$k = \frac{EI}{l} \tag{2.10}$$

where E is the Young's modulus of the material, I is the second moment of area, and l is length of the flexural pivot, as shown in Figure 2.8. Since the material in the fold came from a flat sheet, the compliant model assumes that the cross section of the fold material remains rectangular and the second moment of area is given as

$$I = \frac{bh^3}{12} \tag{2.11}$$

where h and b are the thickness and width of the compliant segment, as shown in Figure 2.8.

Maintaining a symmetry condition requires that all γ_m folds have the same parameter values and fold angles, and the same must be true for all γ_v folds. For the simplest case in which all folds have the same dimensions and therefore the same stiffness k, the total potential energy of the waterbomb base is expressed as

$$V_{TOT} = 2k[(\gamma_m - \gamma_{m0})^2 + (\gamma_v - \gamma_{v0})^2] \tag{2.12}$$

where γ_m and γ_v are functions of θ as defined in equations (2.6)–(2.8) and where γ_{m0} and γ_{v0} are the initial, unstrained angles of the mountain and valley folds, respectively.

For the case in which all mountain folds have the same stiffness k_{γ_m} and all valley folds have stiffness k_{γ_v} but $k_{\gamma_m} \neq k_{\gamma_v}$, the total potential energy becomes

$$V_{TOT} = 2[k_{\gamma_m}(\gamma_m - \gamma_{m0})^2 + k_{\gamma_v}(\gamma_v - \gamma_{v0})^2] \tag{2.13}$$

For either case, once the appropriate k values have been calculated a potential energy plot can be generated by choosing a starting θ_0, determining the associated γ_{m0} and γ_{v0}, then solving equation (2.12) or (2.13) for all values of θ. In the simpler case with only a single k value, this can be simplified by nondimensionalizing (making unitless) equation (2.12) by dividing V_{TOT} by k. Figure 2.9 is one example of a nondimensionalized potential energy plot in which the first stable equilibrium state occurs when θ_0=60°, which corresponds to γ_{m0}=-60° and γ_{v0}=25°. The second stable state occurs when θ=99°, which corresponds

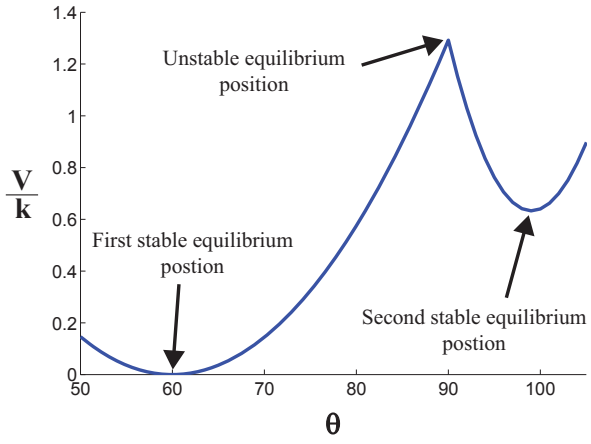

Figure 2.9: Nondimensionalized potential energy plot for θ_0=60°. The two minima are the stable equilibrium positions and the sharp peak is the unstable equilibrium position.

to γ_m=-18° and γ_v=43°. Cases with different k_{γ_m} and k_{γ_v} are considered further in the discussion section.

2.5 Physical prototype

A physical prototype was made of acrylic and metallic glass (see Figure 2.10) to validate the position and potential energy analyses. These materials were selected because acrylic is easy to machine and recent studies have found that bulk metallic glass has favorable properties for use in compliant mechanisms [36]. The rigid sections were laser cut from a 3.175 mm thick sheet of acrylic to create isosceles triangles with two sides measuring 75 mm and the third side measuring 57.4 mm. To ensure that the first stable state was as close to a zero-energy state as possible, the prototype was constructed in the first stable state. This required that the edges at the γ_m joints be cut to 45° angles and those at the γ_v joints be cut to 20° angles so that the joint material would be undeflected at the initial joint angles γ_{m0} and γ_{v0}. The resulting final outer dimensions of the triangles were 71 mm by 71 mm by 56 mm.

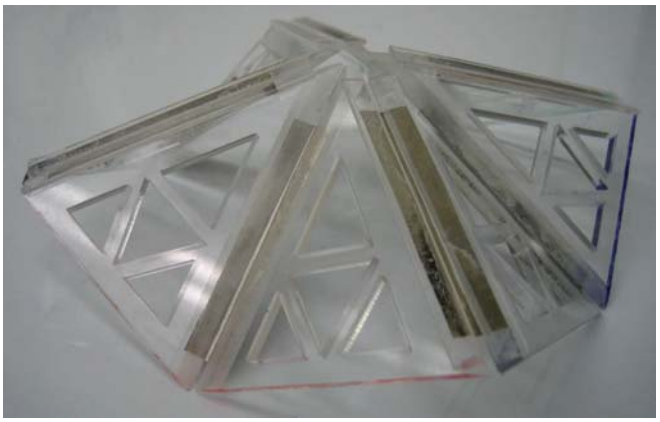

Figure 2.10: Prototype constructed from acrylic and metallic glass

Metallic glass with thickness 0.02 mm and elastic modulus E=93 GPa was used as the small-length flexural pivot. Each strip of metallic glass was 50 mm long by 9 mm wide and was joined to the acrylic sections using a multipurpose adhesive spray.

A fixture held the edges of two adjacent acrylic pieces 0.5 mm apart while the metallic glass was adhered. To account for differences present after assembly, the l dimension was measured at both ends of each joint and the average of all measurements was taken as the nominal value to be used in calculations. The b and h values were measured directly from the metallic glass strips and therefore were not affected by the assembly process. The l, b, and h values were used in equations (2.10) and (2.11) to calculate a stiffness to apply to all joints. These dimensions and the stiffness are listed in Table 2.1.

To avoid delamination of the metallic glass from the acrylic at the γ_m joints, narrow acrylic pieces were adhered over top of the glass (visible in Figure 2.11) to hold it flat up to the edge of the joint and thereby maintain the same geometry throughout the motion.

Table 2.1: Prototype joint dimensions and stiffness.

Dimensions (mm)	l	0.714
	b	50
	h	0.02032
Stiffness (N•m/rad)	k	0.00455

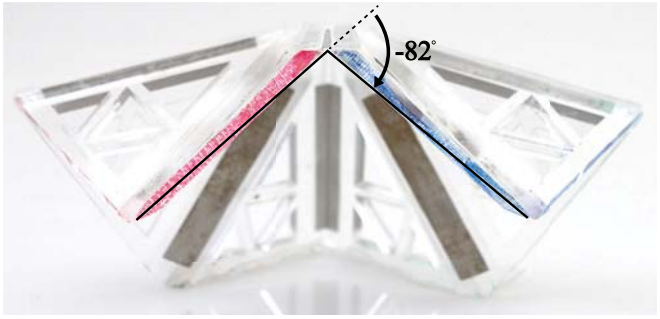

Figure 2.11: Measurement of one γ_m joint on the prototype.

2.5.1 Bistable behavior

The prototype's stable positions were determined by measuring the γ_m and γ_v angles. Photographs of each angle were analyzed to make measurements, as shown in Figure 2.11. To get more accurate results, measurements were taken with the prototype in a variety of orientations and then averaged together to determine the measured γ_m and γ_v angles shown in Table 2.2.

To determine a prediction for the second stable position, the (γ_{m0}, γ_{v0}) pair from the position analysis that was closest to the measured values was used in equation (2.12) to generate a potential energy plot. The value of θ associated with the second local minimum was read off of this plot and then used in equations (2.6) and (2.8) to calculate the (γ_{m1},γ_{v1}) that define the second state. These predicted values are shown on the bottom row of Table 2.2.

Table 2.2: Prototype and predicted angles for bistable positions.

	Position 1		Position 2	
	γ_{m0}	γ_{v0}	γ_{m1}	γ_{v1}
Prototype Angles(°)	-82	32	-20	55
Predicted Angles(°)	-76	32	-24	57

2.5.2 Prototype testing

To gather data from the prototype to compare against the model's predictions, force and deflection data were recorded as the prototype was moved between its stable states using an Instron tabletop tensile testing machine equipped with a Futek LSB200 Load cell. Two tests were conducted: one for Range a and one for Range b. Two tests were done because the points in contact with the lower and upper surfaces switch after the transition through the unstable equilibrium position.

For one test (Range a) the prototype was placed upright on a flat acrylic sheet in the first stable position so that it was resting on the γ_v joints, as shown in Figure 2.12. A flat acrylic surface was chosen because it creates less friction than the test machine's textured metal plate as the joints slide across the surface. The output force was recorded as the vertex was deflected down at a rate of 80 mm/min until the prototype transitioned through the unstable equilibrium position to the second stable position. The other test (Range b) began with the prototype inverted while in the second stable position and placed on acrylic supports so that it was resting on the γ_v joints, as shown in Figure 2.13. A flat sheet was not used for the inverted test because doing so would have left the waterbomb resting on the γ_m joints rather than the γ_v joints, changing the boundary conditions of this test relative to the upright test. As in the upright test, force was recorded as the vertex was deflected down at 80 mm/min until the prototype snapped through to the first stable position.

The data from the upright and inverted prototype tests have been combined into a single plot (Figure 2.14) to make it easier to view the data for the entire motion at once. The upright test data covers the range of $55°{\leq}\theta{\leq}90°$ and the inverted test data is for $90°{\leq}\theta{\leq}105°$.

2.5.3 Energy change comparison

The mechanical work required to move the prototype between stable positions was calculated by integrating the force-deflection data from the tensile tests. The energy changes due to this work and also from the potential energy predictions are plotted against θ in Figure 2.15 for comparison.

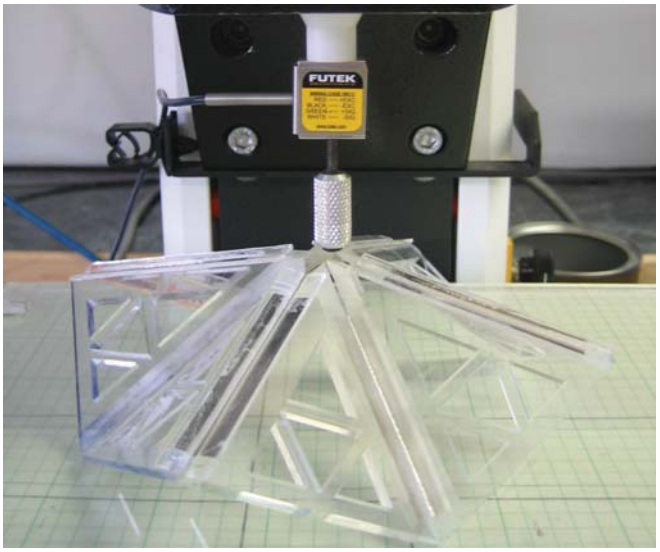

Figure 2.12: Force-displacement testing of the prototype in Range a ($\theta \leq 90°$).

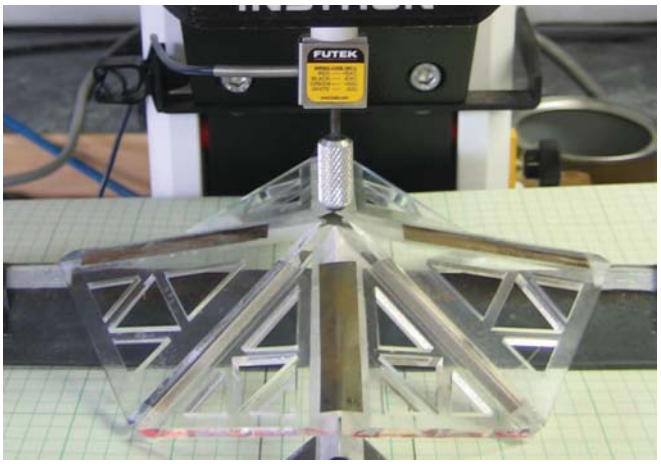

Figure 2.13: Force-displacement testing of the prototype in Range b ($\theta \geq 90°$). The fixture on which the prototype rests ensures that the waterbomb base is supported on the same four joints as in the tests for Range a. The areas that contact the waterbomb base are covered in acrylic to mimic the conditions of the other tests.

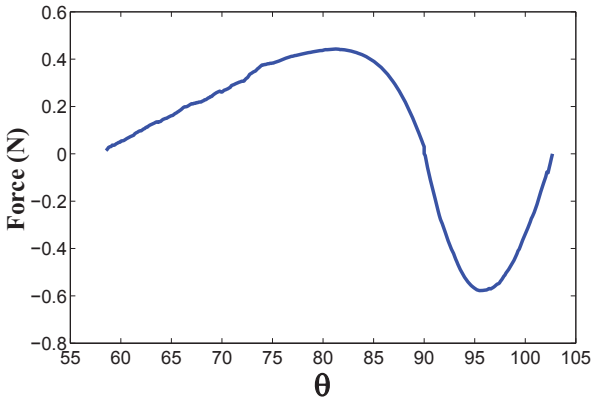

Figure 2.14: Force-deflection curve from prototype tensile testing.

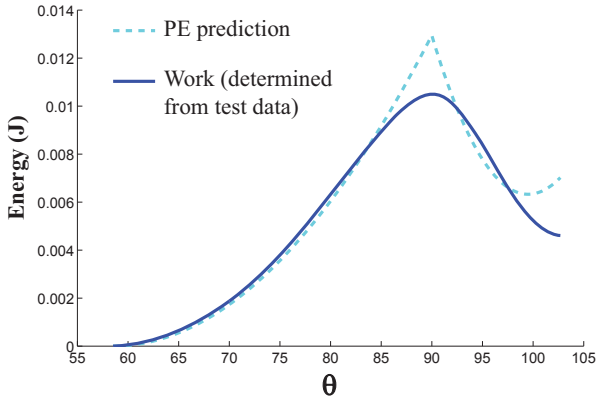

Figure 2.15: Energy changes due to work (as determined from tensile test results) and potential energy storage throughout the waterbomb base's bistable motion.

2.6 Force-deflection behavior

A nonlinear finite element analysis was completed using ANSYS to investigate force-deflection behavior. The finite element model's geometry and dimensions were chosen to match the physical prototype using SHELL281 elements. The properties of the rigid and flexible shell elements are listed in Table 2.3.

To make the analysis similar to the physical tests, the outermost nodes on the γ_v joints were constrained not to move vertically while vertical displacement loads were applied to the innermost nodes of each rigid portion (the vertex of the waterbomb base). The displacement

loads were applied in several load steps until the vertex had been deflected below the plane of the γ_v joints, at which point the final step removed all loads and the mechanism was allowed to converge into its second stable position. Vertical forces and deflections were recorded at each step and are shown in Figure 2.16.

A virtual work analysis was also completed to provide another, simpler means of predicting force-deflection behavior. Using the results of the position analysis and the prototype test geometry as starting points, the principle of virtual work [8] was used to find the following expression for the force:

$$F = \frac{4k[(\gamma_m - \gamma_{m0})\frac{d\gamma_m}{d\theta} + (\gamma_v - \gamma_{v0})\frac{d\gamma_v}{d\theta}]}{r\sin(\theta)} \tag{2.14}$$

where γ_m and γ_v are found in equations (2.6)–(2.8), r is the distance from the vertex to the edge of the waterbomb base measured along a fold (see Figure 2.8), and the kinematic coefficients are defined as

$$\frac{d\gamma_m}{d\theta} = -\frac{4\cos(\theta)\sin(\theta)}{\sin(\gamma_m)} \tag{2.15}$$

$$\begin{aligned} \frac{d\gamma_{va}}{d\theta} &= -\frac{4\cos(\theta)\sin(\theta)}{\sin(c)[\cos(c)+1]\sqrt{1-(\frac{\sin(c)}{\cos(c)+1})^2}} \\ &\quad + \frac{2\cos(\theta)[\sin^2(c) - 2\cos(c)\sin^2(\theta)]}{\sin^3(c)\sqrt{1-(\frac{\sin(\theta)}{\sin(c)})^2}} \end{aligned} \tag{2.16}$$

Table 2.3: Finite element shell element properties.

	Rigid	**Flexible**
Thickness (mm)	3	0.02032
Poisson Ratio	0.35	0.27
Elastic Modulus (MPa)	3.2×10^3	93×10^3

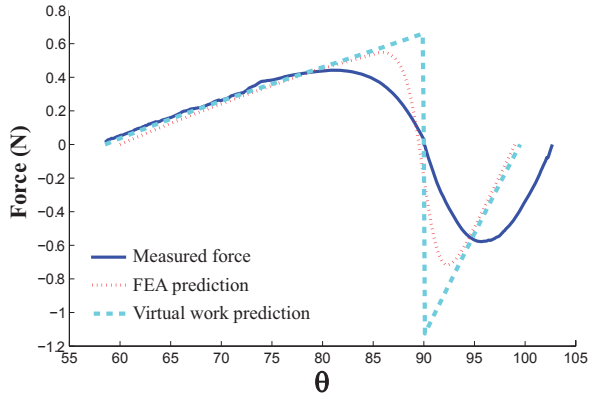

Figure 2.16: Force-deflection behavior measurements, FEA, and analytical predictions.

$$\frac{d\gamma_{vb}}{d\theta} = \frac{2\cos(\theta)}{\sin^3(c)}\left[-\frac{\sin^2(c)-2\cos(c)\sin^2(\theta)}{\sqrt{1-(\frac{\sin(\theta)}{\sin(c)})^2}} + \frac{2\sin(\theta)(\cos(c)-1)}{\sqrt{1-(\csc(c)-\cot(c))^2}}\right] \tag{2.17}$$

where c is defined in equation (2.1). Figure 2.16 shows the force-deflection curves from the measurements, FEA, and virtual work analysis.

Figures 2.15 and 2.16 show that the prototype measurements and the analysis predictions are most similar at values of θ near the first stable position (lowest energy state) and that they differ most in the range θ>90°. These differences in both magnitude and general trend are the result of an imperfect and asymmetric prototype. Since the prototype was manufactured in the first stable position, it is most similar to an ideal waterbomb base when it is closest to this position. Any imperfections are exaggerated the further away from this position it is moved, especially beyond the unstable change point as shown in the force-deflection curves in Figure 2.16. The finite element model is an idealized version of the prototype and therefore it should behave more like a perfect waterbomb base (which was assumed for virtual work) than the prototype.

2.7 Results and discussion

The two stable positions of a waterbomb base do not have the same (γ_m,γ_v) pair or the same energy state even though they look similar at first glance. However, Figure 2.7 helps to illustrate why the positions must be different. For the second stable position to be the same as the first position, both angles must simultaneously return to their original value to return to the lowest potential energy state, which the figure shows is not possible.

When all folds have the same k value and the springs are considered to act within the linear range, the spring constant magnitude influences the forces required to transition the mechanism between stable states as well as the energy required to move the system. It does not, however, affect the equilibrium locations. When all ks are equal, equilibrium locations are determined only by the initial, undeflected position defined by (γ_{m0},γ_{v0}). This is no longer true when k_{γ_m} and k_{γ_v} are allowed to be different.

Figure 2.17 shows potential energy curves that were generated using equation (2.13) with three different k_{γ_m}:k_{γ_v} ratios. Note how the location of the second stable position changes and also how the energy differences between the stable positions vary as the joint stiffnesses are varied. These plots illustrate how changing the joint stiffnesses, which can be as easy as changing the lengths of the folds, can be used to tune the bistable behavior of a waterbomb base. This tunability could make it possible to design waterbomb bases for a variety of applications. Keeping the stable positions as far apart as possible creates bistability that is useful in applications such as switches. On the other hand, moving one stable position very near to the unstable position creates a "cocked" position where the transition between stable states requires a small input, such as in the hair trigger of some firearms.

2.8 Conclusion

A kinematic model was developed that defines the position of a symmetric origami waterbomb base when a single input is known. Predictions of the bistable behavior of the waterbomb base were determined by completing potential energy and finite element analyses of this model, and force-deflection predictions were determined using finite element

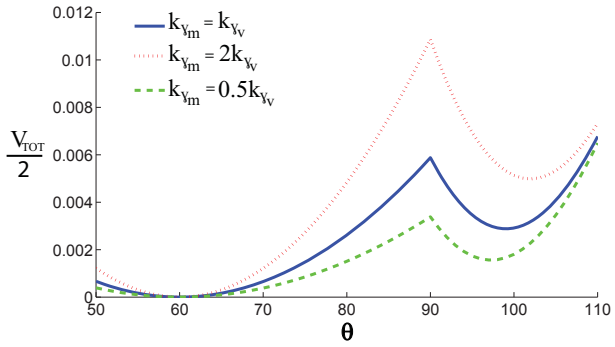

Figure 2.17: Potential energy curves for waterbomb bases with different k_{γ_m}:k_{γ_v} ratios. Note how the second stable position moves as the ratio changes.

analysis and the principle of virtual work. The results were verified through comparison to measurements taken from a physical prototype.

The two stable positions of a waterbomb base are not mirror images of each other and they can be adjusted by changing the stiffness of either the γ_m or the γ_v joints. This tunability could make the waterbomb base useful in a variety of bistable applications or in development of compact nonlinear springs.

The waterbomb base is well suited as a test bed for comparing actuation methods for origami-based systems. Its straightforward topology is manufacturable, transferable, and scalable. It has several phases of motion with varying levels of complexity, including function as a nonlinear spring, bistable mechanism, or bi-directional bistable mechanism. The equations for the motion, force-deflection relationship, and bistable behavior can be helpful in its use as a test bed and for engineering application.

CHAPTER 3. FORCE-DEFLECTION MODELING FOR GENERALIZED ORIGAMI WATERBOMB-BASE MECHANISMS

3.1 Introduction

The origami waterbomb base is a basic origami fold that is attractive for mechanism adaptation due to its straightforward and well-known topology, generalizability, and tunable nonlinear spring and bistable behaviors [37]. The purpose of this work is to derive the kinematic and static force-deflection equations for generalizations of two waterbomb base classes – the generalized waterbomb base (WB) and the generalized split-fold waterbomb base (SFWB). These two classes of mechanisms provide a wider range of kinetic and geometric variety for potential application than the traditional waterbomb base. The traditional waterbomb base is made from a square sheet that has 4 valley folds alternating with 4 mountain folds [21], as shown in Figure 3.1. This particular fold structure has been in use for centuries [19], but the name "waterbomb base" has been applied to it relatively recently [18]. The behavior of the traditional waterbomb base has been modeled [37]. Generalized forms of the waterbomb base (WB) have been made from triangular and hexagonal sheets with 6 and 12 folds, respectively [38], that maintain the pattern of alternating mountain and valley folds, as shown in Figure 3.2. A split-fold waterbomb base (SFWB) is created by splitting each fold of a WB into two "half folds", as shown in Figure 3.3. Because each of these variations of the waterbomb base behaves differently, the general forms add a wider range of tunability to the spring-like and bistable behavior of the original waterbomb base as well as adding greater flexibility to modify geometry, thus expanding the potential utility of these mechanisms.

The waterbomb base is not the first origami fold to inspire a solution to a practical problem. The Miura-ori fold has been considered in the development of deployable solar panels [39] and mechanical metamaterials [17, 40], and has also been found to represent

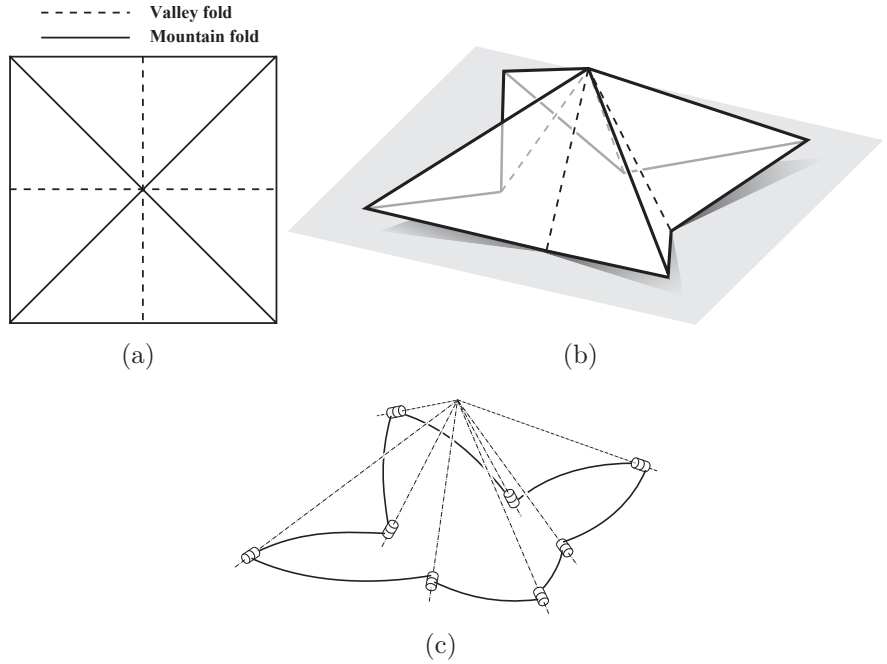

Figure 3.1: (a) Traditional n=4 waterbomb base fold pattern, (b) folded base resting on the flat plane, and (c) spherical mechanism representation.

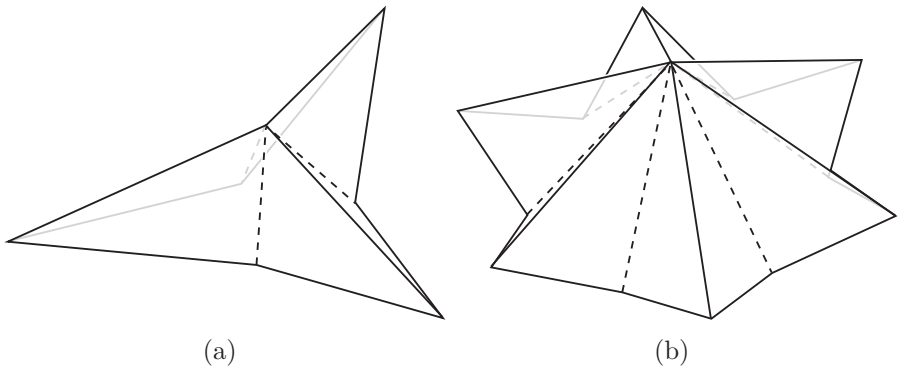

Figure 3.2: (a) n=3 and (b) n=6 waterbomb bases.

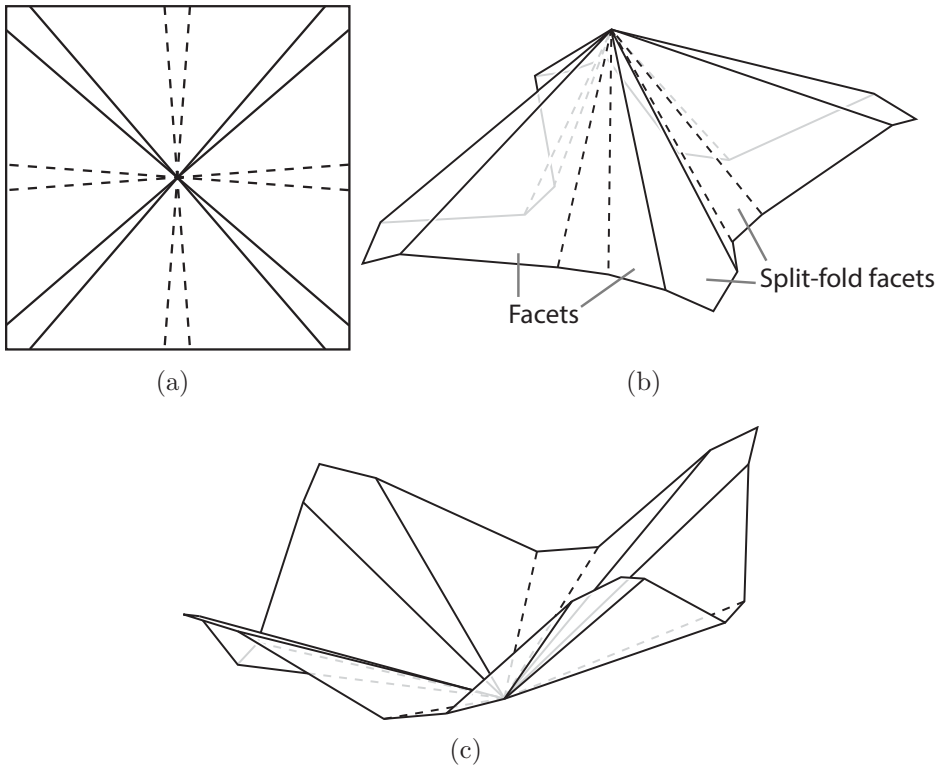

Figure 3.3: Split-fold (a) n=4 waterbomb base fold pattern, (b) line drawing in first stable state, and (c) line drawing in second stable state. Links with different folds on each side (one mountain and one valley) are called facets and those with the same type of fold on both sides (mountain-mountain or valley-valley) are split-fold facets.

one possible natural response to biaxial compression of stiff thin membranes on soft elastic substrates [41]. Other folds have informed the design of deployable arrays [13], collapsing cylinders used in automotive crashboxes [42] and soft robotic actuators [15], and deployable mast structures [43–45] that are based on twisting fold lines that can be viewed from an origami perspective. The idea that a flat sheet can be folded into a wide variety of shapes has inspired the development of programmable matter [46] and self-folding machines [16].

In many technical explorations of origami the mechanisms are modeled as rigid-link systems in which the facets are treated as rigid links and the folds as revolute joints [2, 4, 47, 48], and rigorous mathematical explorations of these types of rigid, non-self-intersecting constructs have also been carried out [49]. Because the folds generally meet at one or several vertices in a given design, the origami can often be kinematically modeled as a series of spherical mechanisms [35, 50]. It is also appropriate to apply the methods of compliant

mechanisms since it is the deflection of the paper at the folds rather than rotation of pins or hinges that enable all motion [8,9]. The compliant mechanism model provides the added benefit of accommodating a wide range of materials. The mechanical response of folded and creased paper materials during deflection has been studied [5,6,27,28] and the crease behavior of non-paper materials has been compared to that of paper for a specific set of materials [7]. Compliant mechanism methods extend that to any material in its elastic range.

The bistable behavior of waterbomb-base-type mechanisms is one point of interest to this study. A bistable mechanism has two stable equilibrium positions at which the potential energy of the mechanism is a local minimum and to which the mechanism tends to move when no external loads are applied [8]. Between these stable positions is an unstable equilibrium position where the mechanism can rest but any slight disturbance will offset the equilibrium and the mechanism will settle into one of the stable states. Bistable mechanisms are common in devices such as light switches and closures. Compliant bistable mechanisms have the ability to use the same flexible members to accomplish both motion and energy storage, eliminating the need for dedicated energy storing components. Such mechanisms have been designed and analyzed in several studies [29–31] and have been suggested as potential candidates for applications as varied as microfluidic microvalves, optical shutter positioners, and zero-power switches and indicators [32, 51, 52].

Previous work [37] has studied an important special case of the waterbomb base with 8 folds (4 mountain and 4 valley). The special case was proposed as a testbed for smart materials and actuation because of its familiarity and straightforward topology, and thus warranted independent in-depth study. While important for use as an actuation testbed, there is a need for broader study to provide understanding of general waterbomb base configurations that will be useful in a broader set of applications. But because of the unique symmetries of the special case (which also make it an important special case), it is nontrivial to extend the analysis to more general configurations. Thus, this chapter describes the general symmetric forms of the waterbomb base and the kinematic, potential energy, and force-deflection analyses are completed for a general number of folds, and the effects that the number of folds has on behavior are explored. The bistable split-fold waterbomb base is also introduced, with its corresponding analyses, including the effect that the relative magnitude

of the split-fold panels has on device behavior. Two application examples are also presented to illustrate some potential uses of the developed models.

3.2 Definition, assumptions, nomenclature for waterbomb base analysis

The waterbomb base (WB) is a single-vertex mechanism with an equal number of alternating mountain and valley folds that can be folded and moved without deflecting any of the facets. A mountain fold exists when the adjacent facets point up out of the flat plane at the fold and a valley fold occurs when the facets point down where they meet, as shown in Figures 3.1(a) and 3.1(b). The WB that is made from a square sheet with 8 folds (4 mountain folds alternating with 4 valley folds going around the vertex) is well known and is a basic fold in origami [21], but variants that are triangular and hexagonal with 6 and 12 folds, respectively, have been used in modern origami and are also considered generalized waterbomb bases [38]. Therefore, in this study the generalized WB is allowed any even number of folds greater than 6 within which there is an equal number of alternating mountain and valley folds.

Simplifying assumptions are:

1. *Developable vertices.* Facet sector angles are assumed to sum to 360° (foldable from a flat sheet). Non-developable waterbomb-like structures can be constructed but doing so requires breaking away from the origami tradition of folding but not cutting.

2. *Rigid foldable.* The mechanism can be folded and moved when the facets are completely rigid. Restricting all motion to the joints simplifies the kinematics compared to a distributed-motion model, and folded paper often follows this behavior fairly closely. Rigid foldability is an important characteristic because it enables extension to non-paper materials.

3. *Rotationally symmetric geometry.* All facets of a waterbomb base have the same sector angle.

4. *Rotationally symmetric motion.* All mountain folds are assumed to be of equal angle at each point in the mechanism's motion, and the same is true for all valley folds. One way

of achieving this motion is by resting a waterbomb base on a flat plane and applying a force at the vertex that is perpendicular to the plane. Although non-symmetric deformations between symmetric states may be energetically preferential in some cases (spontaneous symmetry breaking), those motions also increase the number of degrees of freedom.

The WB can be modeled as a single-degree-of-freedom rigid-link mechanism when each fold is treated as a revolute joint and each facet as a rigid link, and when the WB is symmetric in both geometry and motion. Because all axes of rotation intersect at a common point (the vertex), as shown in Figure 3.1(c), it can also be considered and analyzed as a spherical mechanism [35, 50].

The WB is bistable whenever the undeflected state is non-flat (folds have a non-zero bias) and the hinges operate with elastic behavior. In these cases the mechanism rests in one stable equilibrium state with the vertex pointing in one direction, the unstable equilibrium state occurs when the vertex is deflected such that the paper flattens out, and when the vertex is displaced past the flat plane the mechanism will transition to the second stable state with the vertex pointing in the direction opposite that of the first state.

Fold angles are not measured as the angles between adjacent links but as deviations from straightness across the fold. Therefore an angle of 0° indicates the original, nonfolded flat state. A positive angle indicates folding that brings a facet above the flat sheet, and a negative angle indicates folding a facet below the flat sheet.

Although the mountain and valley folds have different lengths in a waterbomb base, making all of the folds of equal length produces a kinematically equivalent spherical mechanism. Any effects that arise from the different fold lengths will influence the potential energy and force analyses, but these are accounted for by allowing the mountain folds to have a different stiffness than the valley folds.

Finally, since spherical mechanism analysis employs many trigonometric functions, the following shorthand is used to condense the written solutions

$$\mathrm{s}(x) = \sin(x); \qquad \mathrm{c}(x) = \cos(x); \qquad \mathrm{t}(x) = \tan(x);$$

$$\mathrm{cc}(x) = \csc(x); \qquad \mathrm{sc}(x) = \sec(x); \qquad \mathrm{ct}(x) = \cot(x)$$

3.2.1 Waterbomb base nomenclature

The parameter n is used to indicate the degree of the WB where n is equal to the number of mountain folds (or valley folds) present in the folded state. This means that the traditional, square WB has n=4. Figure 3.2 shows n=3 and n=6 WBs.

3.2.2 Split-fold waterbomb bases

To create a split-fold waterbomb base (SFWB), each fold of the WB is split into two "half folds" as shown in Figure 3.3. This creates a "split-fold facet" where there was previously a fold. The sector angle of either a facet or a split-fold facet is chosen, then the sector angle of the other type of link is determined by this angle and n. To maintain a close association with the WB from which each split-fold variant arises, n is now equal to the number of mountain split-fold facets (or valley split-fold facets) rather than the number of folds of each type. In these cases there is an upper bound to n that depends on the sizes of the facets and split-fold facets, but the sum of the sector angles cannot exceed 360°.

The geometric symmetry requirement in the SFWB is adjusted such that all facets must have the same sector angles and the same is true for the split-fold facets, but a facet and a split-fold facet may be different. The symmetric motion assumption is as before.

One reason that SFWBs are attractive is that each joint undergoes a smaller rotation than in the equivalent WB, resulting in lower material strains in the joints. This broadens the range of materials that can be considered for use in the joint. Another reason is that the split-fold facets undergo less complex motions than the facets in a WB, making them easier to interface with in applications. The energy and force behaviors are also different than for a WB, which will be shown in detail later in the chapter.

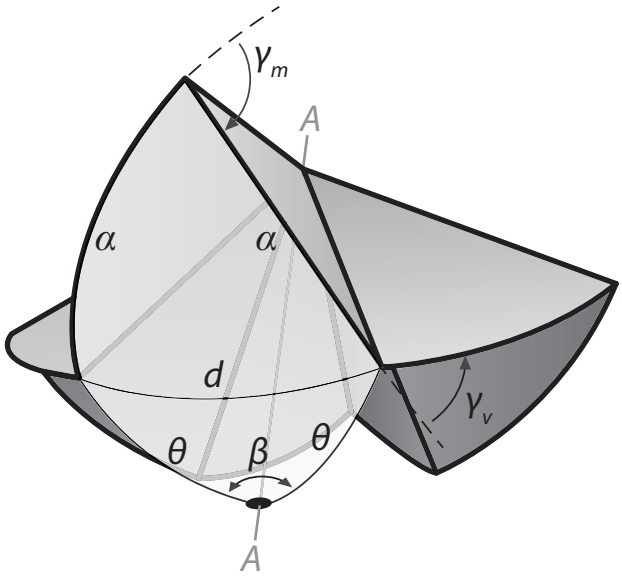

Figure 3.4: Spherical parameters used in WB analysis.

3.3 Waterbomb base (WB) analysis

Taking an approach similar to that used to solve for the traditional n=4 WB in [37], the vertex is assumed to be centered on a circular disk of unit radius and a series of spherical triangles are used to develop a set of analytical solutions for all $n \geq 3$ WBs. The parameters used in the solutions are shown in Figure 3.4. α, d, and θ are the spherical links that form the two spherical triangles and θ also serves as the general coordinate that is measured between any valley fold and the vertical axis A that is perpendicular to the flat plane shown shaded in Figure 3.1(b) and that passes through the vertex.

3.3.1 Position analysis

For a WB of degree n:

$$\alpha = \frac{180^\circ}{n} \tag{3.1}$$

$$\beta = \frac{360^\circ}{n} \tag{3.2}$$

$$0 \leq \theta \leq 180^\circ - \alpha \tag{3.3}$$

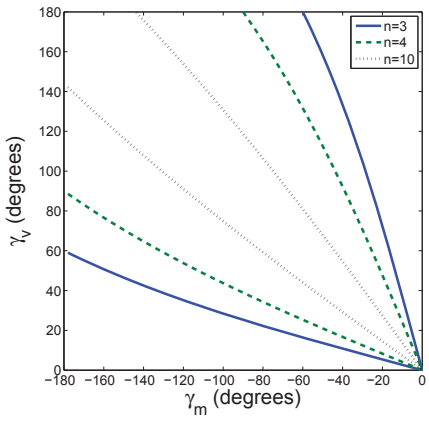

Figure 3.5: Position plots for n=3, n=4, and n=10 waterbomb bases. Note the symmetry about the line passing through (0,0) and (-180,180).

where α is the sector angle of a facet and β is the angle between two folds of the same type (between two mountains or between two valleys) measured about the vertical axis A.

Expressions for the dihedral angles are given as:

$$\gamma_m = -180 + \mathrm{c}^{-1}\left[1 + \frac{\mathrm{c}(d)-1}{\mathrm{s}^2(\alpha)}\right] \tag{3.4}$$

$$\gamma_v = \begin{cases} -180 + 2\mathrm{c}^{-1}\left[\mathrm{ct}(\alpha)\mathrm{t}\left(\frac{d}{2}\right)\right] & \\ \qquad +2\mathrm{c}^{-1}\left[\mathrm{ct}(\theta)\mathrm{t}\left(\frac{d}{2}\right)\right] & : \text{for } \theta \leq 90^\circ \\ 180 - 2\mathrm{c}^{-1}\left[(\mathrm{c}(d)-1)\frac{\mathrm{ct}(\theta)}{\mathrm{s}(d)}\right] & \\ \qquad +2\mathrm{c}^{-1}\left[\mathrm{ct}(\alpha)\mathrm{t}\left(\frac{d}{2}\right)\right] & : \text{for } \theta > 90^\circ \end{cases} \tag{3.5}$$

with

$$d = \mathrm{c}^{-1}[\mathrm{c}^2(\theta) + \mathrm{s}^2(\theta)\mathrm{c}(\beta)] \tag{3.6}$$

Figure 3.5 shows the mountain and valley fold angles for the full range of motion of n=3, n=4, and n=10 WBs. Figure 3.6 shows the valley and mountain fold angles (γ_m and γ_v) plotted against θ to show their relations to the generalized coordinate. 3D CAD models

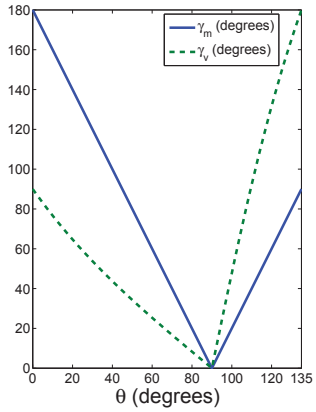

Figure 3.6: γ_m and γ_v plotted against θ for an n=4 WB.

were built of a several different WBs to compare against the analytical model's predictions. Multiple positions were checked for each model, and all positions matched the predictions well.

3.3.2 Potential energy analysis

To solve for the potential energy behavior, each fold is approximated as a revolute joint with a zero-length torsional spring. The potential energy, V, for one of these joints is

$$V = \frac{1}{2}k(\Theta)^2 \tag{3.7}$$

where k is the stiffness and Θ is the angle of deflection of the joint. Therefore, a waterbomb base with n mountain folds and n valley folds has a total potential energy of

$$V_{TOT} = \frac{n}{2}[k_{\gamma_m}(\gamma_m - \gamma_{m0})^2 + k_{\gamma_v}(\gamma_v - \gamma_{v0})^2] \tag{3.8}$$

where γ_{m0} and γ_{v0} are the angles associated with the undeflected state at θ_0 and the stiffnesses k are related to the material, sheet thickness, and length of the fold. Although zero-length torsional springs were used here, the folds could also be modeled as compliant conical sections or rectangular sections, as described in [37].

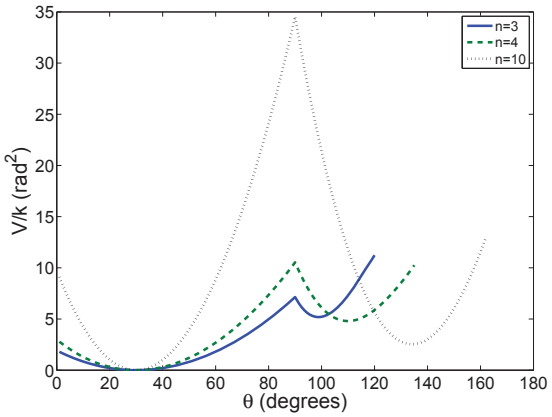

Figure 3.7: Potential energy plots for n=3, n=4, and n=10 waterbomb bases where θ_0=30° and the stiffnesses of the mountain folds and valley folds are equal. The potential energy is divided by the stiffness to facilitate comparison.

The potential energy curves for three WBs of different degree n but same θ_0 are shown in Figure 3.7. Note that since the unstable state occurs at θ=90° (the flat state), the initial, undeflected state must occur somewhere else or there will be no bistability. θ_0 was chosen to be 30° here, but any valid θ could have been used. The energy behavior presented in the figure is not dependent solely on the degree of the WB, however. Equation 3.8 shows that the stiffness ratio k_{γ_m}:k_{γ_v} as well as the undeflected angles γ_{m0} and γ_{v0} affect the shape of the energy curve. The effects of adjusting these variables will be discussed later on.

3.3.3 Force-deflection behavior

The principle of virtual work was used to analyze the force-deflection behavior for the waterbomb base that is vertically supported on the outermost points of the valley folds while a vertical force deflects the vertex, as shown in Figure 3.8. The force-deflection behavior is

$$\begin{aligned} F &= -\frac{dV}{d\theta}\frac{d\theta}{dh} \\ F &= \frac{n[k_{\gamma_m}(\gamma_m-\gamma_{m0})\frac{d\gamma_m}{d\theta}+k_{\gamma_v}(\gamma_v-\gamma_{v0})\frac{d\gamma_v}{d\theta}]}{\mathrm{s}(\theta)r} \end{aligned} \tag{3.9}$$

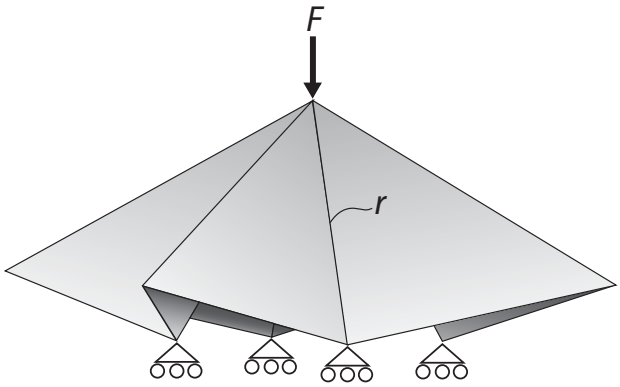

Figure 3.8: Boundary conditions for the force-deflection analysis of the n=4 WB. A vertical force is applied at the vertex while the outermost points of the valley folds are vertically supported.

where h=cos(θ)r is the height of the waterbomb base, r is the distance from the vertex to a support point measured along a fold (see Figure 3.8), and the kinematic coefficients are

$$\frac{d\gamma_m}{d\theta} = [\mathrm{c}(\beta)-1]\mathrm{s}(2\theta)\mathrm{cc}^2(\alpha)\mathrm{cc}(\gamma_m) \tag{3.10}$$

$$\begin{aligned}\frac{d\gamma_v}{d\theta} &= 2\mathrm{cc}(d)[\mathrm{c}(d)-1] \\ &\quad \times \left[\frac{\mathrm{ct}(\alpha)\mathrm{cc}(d)\frac{dd}{d\theta}}{\sqrt{1-\mathrm{ct}^2(\alpha)\mathrm{t}^2(\frac{d}{2})}}\right. \\ &\quad \left. + \frac{\mathrm{ct}(\theta)\mathrm{cc}(d)\frac{dd}{d\theta}-\mathrm{cc}^2(\theta)}{\sqrt{1-\mathrm{ct}^2(\theta)\mathrm{t}^2(\frac{d}{2})}}\right]\end{aligned} \tag{3.11}$$

$$\frac{dd}{d\theta} = \frac{\mathrm{s}(2\theta)[1-\mathrm{c}(\beta)]}{\mathrm{s}(d)} \tag{3.12}$$

The force-deflection curves for three WBs are given in Figure 3.9.

To validate these WB models the results for an n=4 WB were compared to the experimental results given in [37] and found to match reasonably well.

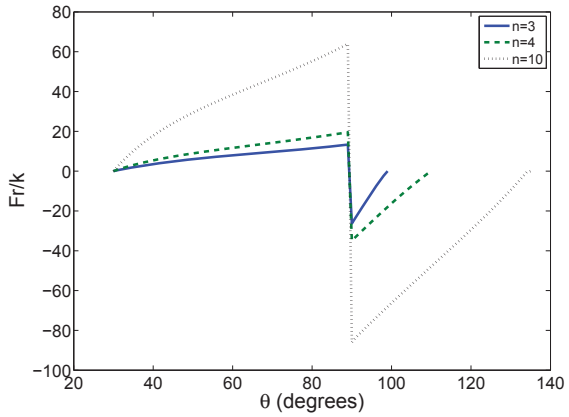

Figure 3.9: Non-dimensionalized force-deflection plots for n=3, n=4, and n=10 waterbomb bases.

3.3.4 Effects of varying θ_0

Up to this point, WBs of different degree but same initial general coordinate (θ_0) have been compared, but it is important to note that varying θ_0 while holding everything else constant can have significant effects. To illustrate some of these effects, θ_0 was chosen for n=3 and n=10 WBs such that the arithmetic average of the initial mountain and valley folds, γ_{m0} and γ_{v0}, is the same. The resulting potential energy and force-deflection relationships are shown in Figure 3.10.

3.4 Split-fold waterbomb base (SFWB) analysis

A series of spherical triangles and spherical fourbars was used to develop a set of solutions for $n\geq$3 SFWBs. The parameters used in the solutions are shown in Figure 3.11. For the SFWBs, the general coordinate θ is measured between the centerline of a valley split-fold facet and the vertical axis A that passes through the vertex and is perpendicular to the flat plane.

3.4.1 Position analysis

Because there are two different links present, the size of one must be chosen to set the geometry. α is the sector angle of the facets, b is the sector angle of the split-fold facets, and

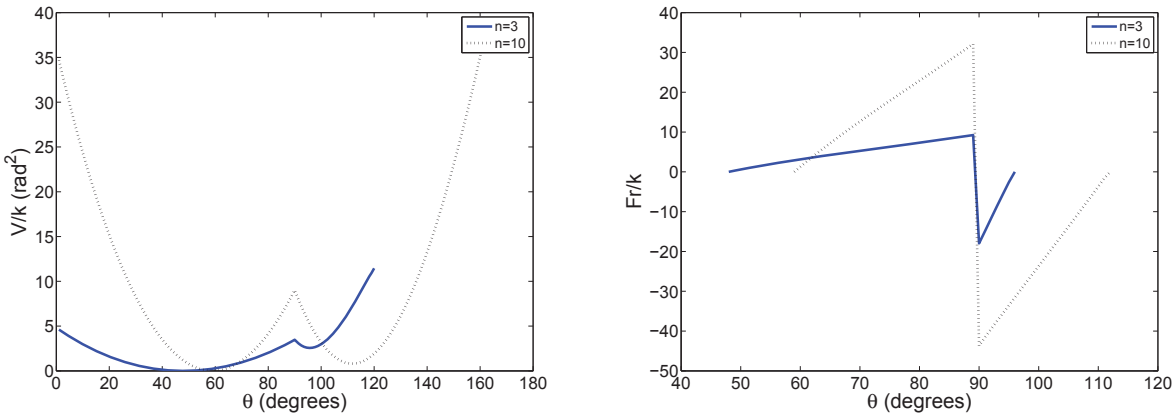

(a) (b)

Figure 3.10: (a) Potential energy and (b) force deflection plots for n=3 and n=10 WBs for which the average of the initial angles γ_{m0} and γ_{v0} is 54°. For the n=3 WB, this average occurs at θ_0=48° and for the n=10 WB it occurs at θ_0=54°.

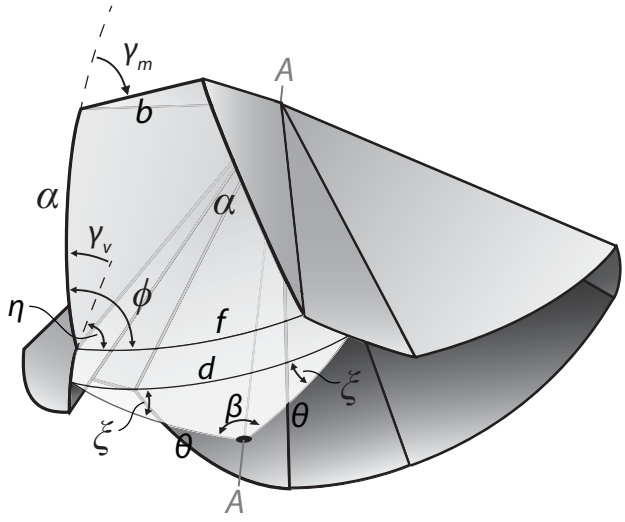

Figure 3.11: Spherical parameters used to analyze SFWBs.

β is the angle between the center points of "neighboring" split-fold facets measured about the axis A.

If b is chosen first, then

$$\alpha = \frac{180^\circ - nb}{n} \tag{3.13}$$

$$\beta = \frac{360^\circ}{n} \tag{3.14}$$

The angle of each mountain fold is given as:

$$\gamma_m = -\mathrm{c}^{-1}\left\{\mathrm{cc}(\alpha)\mathrm{sc}\left(\frac{b}{2}\right)\mathrm{s}\left(\frac{f}{2}\right) - \mathrm{ct}(\alpha)\mathrm{t}\left(\frac{b}{2}\right)\right\} \tag{3.15}$$

which requires

$$\begin{aligned} f &= \mathrm{c}^{-1}\left\{\mathrm{c}^2\left(\frac{b}{2}\right)\mathrm{c}(d) + \mathrm{s}(b)\mathrm{s}(d)\mathrm{s}(\xi)\right. \\ &\qquad \left. + \mathrm{s}^2\left(\frac{b}{2}\right)\left[\mathrm{c}^2(\xi) - \mathrm{c}(d)\mathrm{s}^2(\xi)\right]\right\} \qquad (3.16) \\ d &= \mathrm{c}^{-1}\{\mathrm{c}^2(\theta) + \mathrm{s}^2(\theta)\mathrm{c}(\beta)\} \qquad (3.17) \\ \xi &= \mathrm{c}^{-1}\left\{\mathrm{ct}(\theta)\mathrm{t}\left(\frac{d}{2}\right)\right\} \qquad (3.18) \end{aligned}$$

The above expressions hold for the full range of motion.

The valley fold angles are

$$\gamma_v = \begin{cases} \phi - \eta & : \theta \leq 90^\circ \\ \phi + \eta & : \theta > 90^\circ \end{cases} \tag{3.19}$$

where ϕ and η are

$$\phi = 180^\circ - \mathrm{c}^{-1}\left\{\mathrm{cc}(\alpha)\mathrm{sc}\left(\frac{f}{2}\right)\mathrm{s}\left(\frac{b}{2}\right) - \mathrm{ct}(\alpha)\mathrm{t}\left(\frac{f}{2}\right)\right\} \tag{3.20}$$

$$\eta = 2\tan^{-1}\left\{\frac{-{h_3}^* + \sqrt{{h_3}^{*2} - {h_1}^{*2} + {h_2}^{*2}}}{{h_1}^* - {h_2}^*}\right\} \tag{3.21}$$

with f defined in (3.16) and

$${h_1}^* = {k_1}^* - {k_2}^* + \mathrm{s}(\xi){k_3}^* \tag{3.22}$$

$${h_2}^* = -{k_4}^* + \mathrm{s}(\xi){k_5}^* \tag{3.23}$$

$${h_3}^* = \begin{cases} \mathrm{c}(\xi){k_6}^* & : \theta \leq 90^\circ \\ -\mathrm{c}(\xi){k_6}^* & : \theta > 90^\circ \end{cases} \tag{3.24}$$

where

$${k_1}^* = \mathrm{c}(d)\mathrm{c}(f)\mathrm{c}\left(\frac{b}{2}\right) \tag{3.25}$$

$${k_2}^* = \mathrm{c}\left(\frac{b}{2}\right) \tag{3.26}$$

$${k_3}^* = \mathrm{s}(d)\mathrm{c}(f)\mathrm{s}\left(\frac{b}{2}\right) \tag{3.27}$$

$${k_4}^* = \mathrm{c}(d)\mathrm{s}(f)\mathrm{s}\left(\frac{b}{2}\right) \tag{3.28}$$

$${k_5}^* = \mathrm{s}(d)\mathrm{s}(f)\mathrm{c}\left(\frac{b}{2}\right) \tag{3.29}$$

$${k_6}^* = \mathrm{s}(d)\mathrm{s}(f) \tag{3.30}$$

Position plots for three different SFWBs are given in Figure 3.12. As an initial verification, 3D CAD models were built of a few different SFWBs to compare against the analytical model's predictions. For each point checked, the 3D and analytical models matched up well.

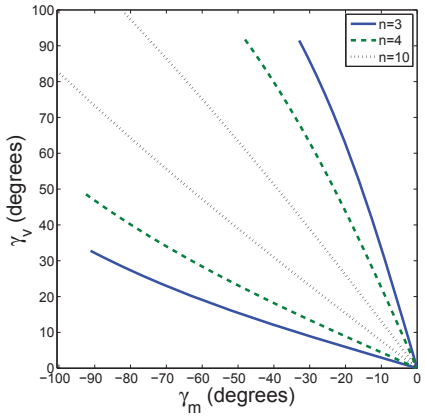

Figure 3.12: Position plots for n=3, n=4, and n=10 split-fold waterbomb bases with b=5°. Note the symmetry about the line passing through (-100,100) and (0,0).

3.4.2 Potential energy analysis

As in the previous case, each fold is considered to be a small-length flexural pivot of rectangular cross section, resulting in the total potential energy, V_{TOT}, of

$$V_{TOT} = n\left[k_{\gamma_m}(\gamma_m - \gamma_{m0})^2 + k_{\gamma_v}(\gamma_v - \gamma_{v0})^2\right] \tag{3.31}$$

The potential energy curves for three SFWBs are shown in Figure 3.13.

3.4.3 Force-deflection behavior

The force-deflection behavior was analyzed with a vertical force applied to the vertex while the waterbomb base is vertically supported at the centers of the outer edges of the valley split-fold facets, as shown in Figure 3.14. The resulting force-deflection relationship is

$$\begin{aligned} F &= -\frac{dV}{d\theta}\frac{d\theta}{dh} \\ F &= \frac{2n\left[k_{\gamma_m}(\gamma_m - \gamma_{m0})\frac{d\gamma_m}{d\theta} + k_{\gamma_v}(\gamma_v - \gamma_{v0})\frac{d\gamma_v}{d\theta}\right]}{\mathrm{s}(\theta)r} \end{aligned} \tag{3.32}$$

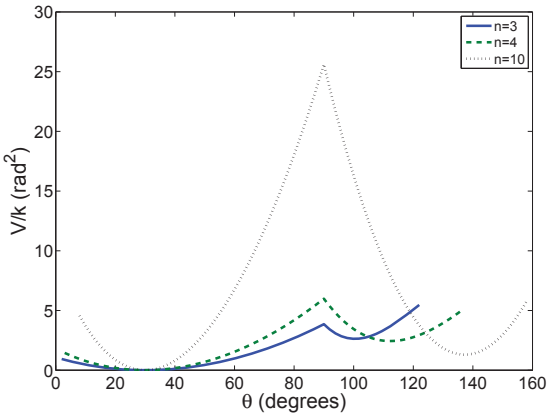

Figure 3.13: Potential energy plots for n=3, n=4, and n=10 split-fold waterbomb bases where b=5° and θ_0=30°. The strain energy is nondimensionalised by dividing out the stiffness k, where k=$k_{\gamma m}$=$k_{\gamma v}$.

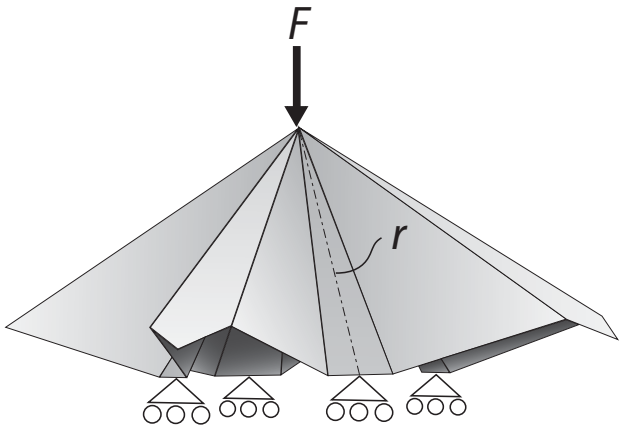

Figure 3.14: Boundary conditions for the split-fold force-deflection analysis. A vertical force is applied at the vertex while the midpoints of the valley split-fold facets are vertically supported.

where h=cos(θ)r is the height of the waterbomb base, r is the distance from the vertex to the point of support, and the kinematic coefficients are

$$\frac{d\gamma_m}{d\theta} = \frac{\mathrm{cc}\left(\alpha\right)\mathrm{sc}\left(\frac{b}{2}\right)\mathrm{c}\left(\frac{f}{2}\right)\frac{df}{d\theta}}{2\sqrt{1-\left\{\mathrm{cc}(\alpha)\mathrm{sc}\left(\frac{b}{2}\right)\mathrm{s}\left(\frac{f}{2}\right)-\mathrm{ct}(\alpha)\mathrm{t}\left(\frac{b}{2}\right)\right\}^2}} \tag{3.33}$$

$$\frac{d\gamma_v}{d\theta} = \begin{cases} \frac{d\phi}{d\theta}-\frac{d\eta}{d\theta} & :\theta \le 90^\circ \\ \frac{d\phi}{d\theta}+\frac{d\eta}{d\theta} & :\theta > 90^\circ \end{cases} \tag{3.34}$$

with the following derivatives:

$$\begin{aligned} \frac{df}{d\theta} = \frac{1}{A}\Bigg\{ & \mathrm{c}^2\left(\frac{b}{2}\right)\mathrm{s}(d)\frac{dd}{d\theta} \\ & -\mathrm{s}(b)\left[\mathrm{s}(d)\mathrm{c}(\xi)\frac{d\xi}{d\theta}+\mathrm{s}(\xi)\mathrm{c}(d)\frac{dd}{d\theta}\right] \\ & -\mathrm{s}^2\left(\frac{b}{2}\right)\mathrm{s}(\xi)\Bigg[-2\left[1+\mathrm{c}(d)\right]\mathrm{c}(\xi)\frac{d\xi}{d\theta} \\ & +\mathrm{s}(\xi)\mathrm{s}(d)\frac{dd}{d\theta}\Bigg]\Bigg\} \end{aligned} \tag{3.35}$$

$$\begin{aligned} A = \Bigg\{ & 1-\Bigg[\mathrm{c}^2\left(\frac{b}{2}\right)\mathrm{c}(d)+\mathrm{s}(b)\mathrm{s}(d)\mathrm{s}(\xi) \\ & +\mathrm{s}^2\left(\frac{b}{2}\right)\left[\mathrm{c}^2(\xi)-\mathrm{c}(d)\mathrm{s}^2(\xi)\right]\Bigg]^2\Bigg\}^{1/2} \end{aligned} \tag{3.36}$$

$$\frac{dd}{d\theta} = \frac{-\mathrm{s}(2\theta)[\mathrm{c}(\beta)-1]}{\mathrm{s}(d)} \tag{3.37}$$

$$\frac{d\xi}{d\theta} = \frac{\left[1-2\mathrm{c}(2d)+\mathrm{c}(\beta)+2\mathrm{c}(4\theta)\mathrm{s}^2\left(\frac{\beta}{2}\right)\right]\mathrm{t}\left(\frac{d}{2}\right)}{4\mathrm{s}^2(d)\mathrm{s}^2(\theta)\mathrm{s}(\xi)} \tag{3.38}$$

$$\frac{d\phi}{d\theta} = \frac{\mathrm{sc}\left(\frac{f}{2}\right)\left[\mathrm{cc}(\alpha)\mathrm{s}\left(\frac{b}{2}\right)\mathrm{t}\left(\frac{f}{2}\right)-\mathrm{ct}(\alpha)\mathrm{sc}\left(\frac{f}{2}\right)\right]\frac{df}{d\theta}}{2\sqrt{1-\left[\mathrm{cc}(\alpha)\mathrm{sc}\left(\frac{f}{2}\right)\mathrm{s}\left(\frac{b}{2}\right)-\mathrm{ct}(\alpha)\mathrm{t}\left(\frac{f}{2}\right)\right]^2}} \tag{3.39}$$

$$\begin{aligned} \frac{d\eta}{d\theta} = & \frac{2}{[h_1{}^*-h_2{}^*]^2\left[\left\{\frac{-h_3{}^*+B}{h_1{}^*-h_2{}^*}\right\}^2+1\right]}\left\{[h_1{}^*-h_2{}^*]\right. \\ & \times\left[\frac{1}{B}\left(h_3{}^*\frac{dh_3{}^*}{d\theta}-h_1{}^*\frac{dh_1{}^*}{d\theta}+h_2{}^*\frac{dh_2{}^*}{d\theta}\right)\right. \\ & \left.\left.-\frac{dh_3{}^*}{d\theta}\right]-[B-h_3{}^*]\left[\frac{dh_1{}^*}{d\theta}-\frac{dh_2{}^*}{d\theta}\right]\right\} \end{aligned} \tag{3.40}$$

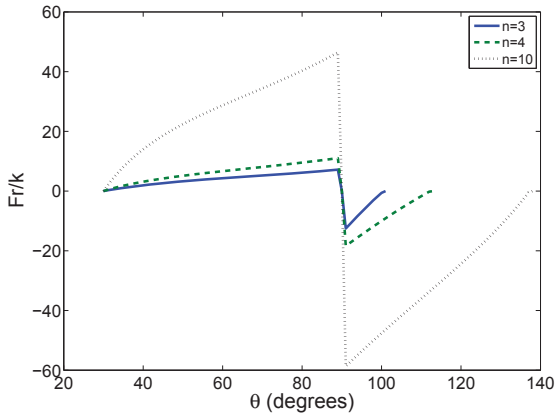

Figure 3.15: Non-dimensionalized force-deflection plots for n=3, n=4, and n=10 split-fold waterbomb bases with b=5° and θ_0=30°.

$$B = \sqrt{{h_3}^{*2} - {h_1}^{*2} + {h_2}^{*2}} \tag{3.41}$$

$$\frac{d{h_1}^*}{d\theta} = \frac{d{k_1}^*}{d\theta} + {k_3}^*\mathrm{c}(\xi)\frac{d\xi}{d\theta} + \mathrm{s}(\xi)\frac{d{k_3}^*}{d\theta} \tag{3.42}$$

$$\frac{d{h_2}^*}{d\theta} = -\frac{d{k_4}^*}{d\theta} + {k_5}^*\mathrm{c}(\xi)\frac{d\xi}{d\theta} + \mathrm{s}(\xi)\frac{d{k_5}^*}{d\theta} \tag{3.43}$$

$$\frac{d{h_3}^*}{d\theta} = \begin{cases} -{k_6}^*\mathrm{s}(\xi)\frac{d\xi}{d\theta} + \mathrm{c}(\xi)\frac{d{k_6}^*}{d\theta} & : \theta \leq 90° \\ {k_6}^*\mathrm{s}(\xi)\frac{d\xi}{d\theta} - \mathrm{c}(\xi)\frac{d{k_6}^*}{d\theta} & : \theta > 90° \end{cases} \tag{3.44}$$

$$\frac{d{k_1}^*}{d\theta} = -\mathrm{c}\left(\frac{b}{2}\right)\left[\mathrm{c}(d)\mathrm{s}(f)\frac{df}{d\theta} + \mathrm{s}(d)\mathrm{c}(f)\frac{dd}{d\theta}\right] \tag{3.45}$$

$$\frac{d{k_3}^*}{d\theta} = -\mathrm{s}\left(\frac{b}{2}\right)\left[\mathrm{s}(d)\mathrm{s}(f)\frac{df}{d\theta} - \mathrm{c}(d)\mathrm{c}(f)\frac{dd}{d\theta}\right] \tag{3.46}$$

$$\frac{d{k_4}^*}{d\theta} = \mathrm{s}\left(\frac{b}{2}\right)\left[\mathrm{c}(d)\mathrm{c}(f)\frac{df}{d\theta} - \mathrm{s}(d)\mathrm{s}(f)\frac{dd}{d\theta}\right] \tag{3.47}$$

$$\frac{d{k_5}^*}{d\theta} = \mathrm{c}\left(\frac{b}{2}\right)\left[\mathrm{s}(d)\mathrm{c}(f)\frac{df}{d\theta} + \mathrm{c}(d)\mathrm{s}(f)\frac{dd}{d\theta}\right] \tag{3.48}$$

$$\frac{d{k_6}^*}{d\theta} = \mathrm{s}(d)\mathrm{c}(f)\frac{df}{d\theta} + \mathrm{c}(d)\mathrm{s}(f)\frac{dd}{d\theta} \tag{3.49}$$

The force-deflection curves for three SFWBs are given in Figure 3.15.

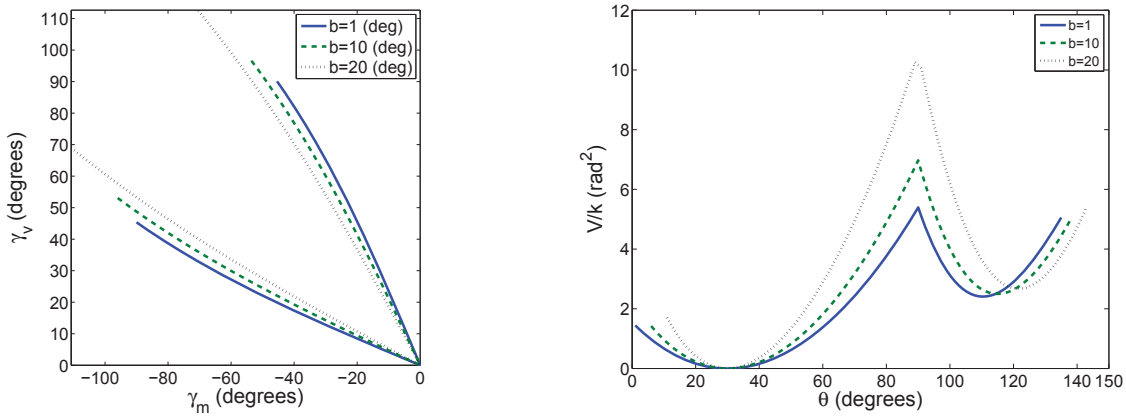

(a) (b)

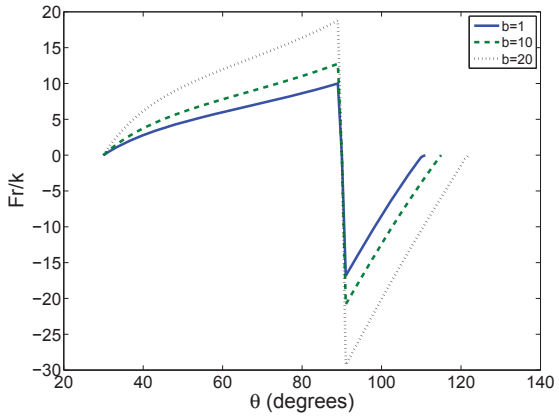

(c)

Figure 3.16: (a) Position, (b) potential energy, and (c) force-deflection plots for b=1°, b=10°, and b=20° SFWBs where n=4 and θ_0=30°.

3.4.4 Further tunability

It was shown in previous sections that the general forms of the waterbomb base are tunable by varying the degree of the base n as well as by adjusting the stiffness ratio k_{γ_m}:k_{γ_v}. The SFWB has another layer of tunability, however. This added control is accomplished by varying the split-fold facet's sector angle b. Figure 3.16 illustrates this with position, potential energy, and force-deflection plots for SFWBs of the same degree and θ_0 but different values of b.

3.5 Results and discussion

One of the assumptions used was that all joints operate elastically, and these results can be used to ensure that a given design meets this assumption. The position plots like those given in Figures 3.5, 3.12, and 3.16(a) show the maximum deflections the folds can experience as the mechanism switches between stable states. These deflections are related to the stresses the joints experience, and this can be used to modify the design such that the elastic range of behavior is not exceeded.

The WB and SFWB have similarly tunable bistable and force-deflection behavior. By adjusting the stiffness ratio k_{γ_m}:k_{γ_v}, the second stable state can be moved closer to the unstable state to create a "cocked" position that requires only a small input to trigger the switch, or it can be moved further away from the unstable state to create a second stable state more like the first as shown in [37]. Also, the lower the degree n of the WB or SFWB, the closer the second stable state will be to the unstable state. Therefore if the goal is a cocked position, a low-degree mechanism is preferred. If, however, the objective is to have more distance between the stable and unstable equilibrium states, the higher the degree the better.

Another feature common to both the WB and SFWB is that if k_{γ_m}=k_{γ_v}, the equilibrium locations are not affected by the magnitude of the torsional spring constant and the equilibrium states are determined by the undeflected state (γ_{m0},γ_{v0}) and the mechanism geometry.

The models predict that, for all mechanisms considered here, the higher the degree of the mechanism, the greater the potential energy and force involved in moving it around and between its stable states. As the degree increases, the number of folds goes up while the range of motion of each fold decreases. These two results have competing effects as a higher number of active elements raises required force and energy while a lower active range of motion for each element reduces those kinetic quantities. In the cases considered here, the reducing effects of the higher degree's reduced motion are not enough to offset the increases from raising the number of folds. Therefore, the net effect is an increase in potential energy and force as the degree of the mechanism is increased.

The SFWB has an added layer of adjustability due to the presence of split-fold facets. Changing the sector angle of the split-fold facets, b, affects the final position solution in addition to the bistable properties and force-deflection behavior. This means that for a given SFWB of degree n and stiffness ratio k_{γ_m}:k_{γ_v}, the solution set will be different for every split-fold facet sector angle b. A comparison of the vertical axes of Figures 3.13 and 3.16(b) as well as of Figures 3.15 and 3.16(c) suggest that varying the degree n of the SFWB may be best for coarse tuning of the mechanism and varying the split-fold facet angle b may be good for smaller, finer adjustments. This provides for greater customizability than a WB possesses in a broad range of potential applications.

The decision between using a WB or an SFWB can be influenced by several factors. SFWBs tend to involve lower forces and potential energy magnitudes than the equivalent WBs, so they may be better suited to sensitive applications. Geometry must also be considered, especially when the waterbomb base will be interfacing with other components. All facets on a WB undergo translation in two directions and rotation in two directions as the mechanism moves. On an SFWB the split-fold facets also translate in two directions but rotate in only one direction. The difference of one extra rotation makes interfacing with an SFWB's split-fold facet easier than a WB's facet.

The models presented here are for symmetric configurations and motions. One of the reasons that these cases were chosen is that they are often empirically observed. If a symmetric waterbomb base is folded, rested on a horizontal surface, and a vertical force is applied at the vertex, symmetric motion is the result. Since strain energy varies with the change in angle squared, as indicated in (3.8) and (3.31), this symmetric motion will also keep strain energy levels at a minimum in most cases as it minimizes the average deviation away from the undeflected state. This is not to say that symmetry will always result in the lowest energy, however. There could be instances in which non-symmetric motion could be energetically preferential, particularly in a higher-degree waterbomb base.

The results are expected to be helpful in designing for applications. A few illustrative examples are described briefly here. The first is the use of the WBs as a testbed for actuation. There are several common testbeds [37] for actuation techniques such as the folding box [22–25]. Arrays of WBs could provide new mechanisms to be actuated. For example, rather

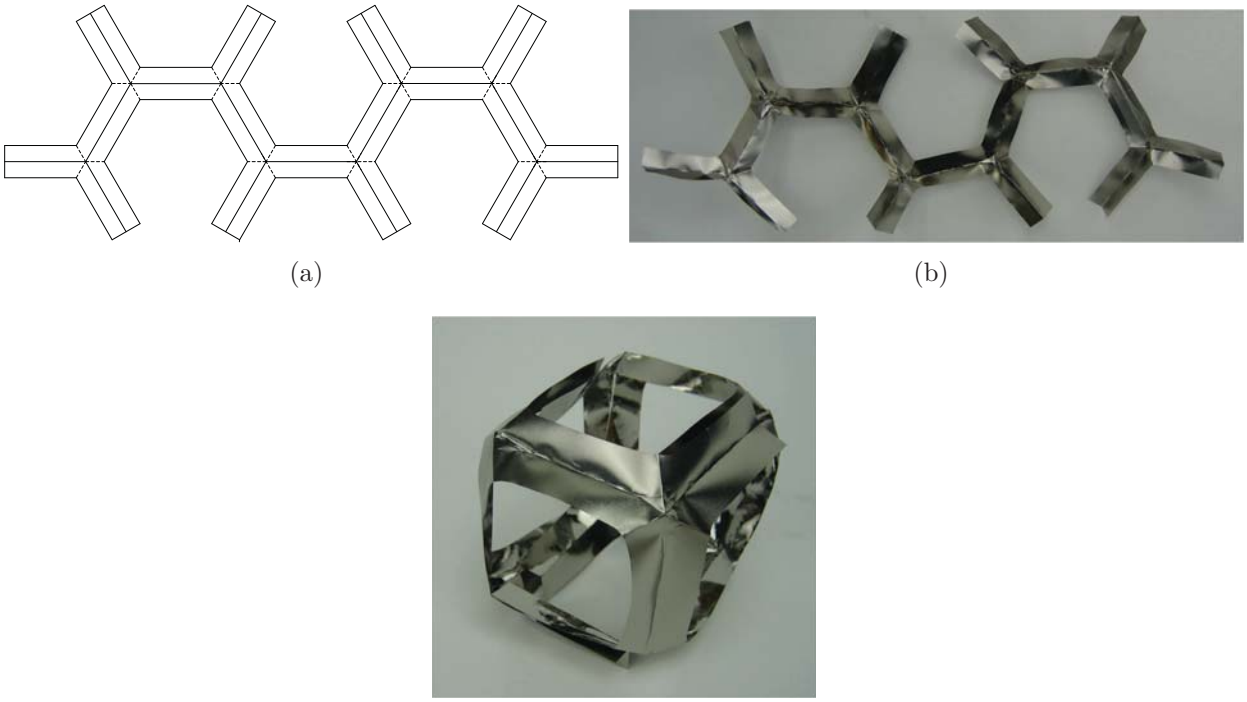

(a) (b) (c)

Figure 3.17: Actuation testbed example (a) flat pattern, (b) metallic glass prototype in nearly flat state, and (c) prototype in erect state. The nearly flat state occurs when all WBs are in one stable state and the erect state occurs when all WBs are switched to the other stable state. Although a cube only has 12 edges, this pattern has 17 links. The extra links enable overlap for additional stability in the erect state.

than folding a flat pattern into a box, a series of n=3 WBs could be designed to fold from a roughly flat array in one state to the edge profile of a box when all WBs are in the other stable state, as shown in Figure 3.17. The prototype in the figure was made from metallic glass, which shows promise as a new compliant mechanism material [36]. Other examples of potential actuation applications are "digital origami" strips and sheets, as shown in Figures 3.18 and 3.19, respectively, in which the waterbomb bases act as digital unit elements that are turned "on" or "off" to contribute to the global shape of the sheet or strip.

As another example, different degrees of SFWB could be designed to grip specific objects. The degree of the base could be chosen based upon the geometry of the object to be gripped and the actual gripping surfaces could be almost any shape. In one stable state the gripper would be open and in the other state it would be closed, but the amount of

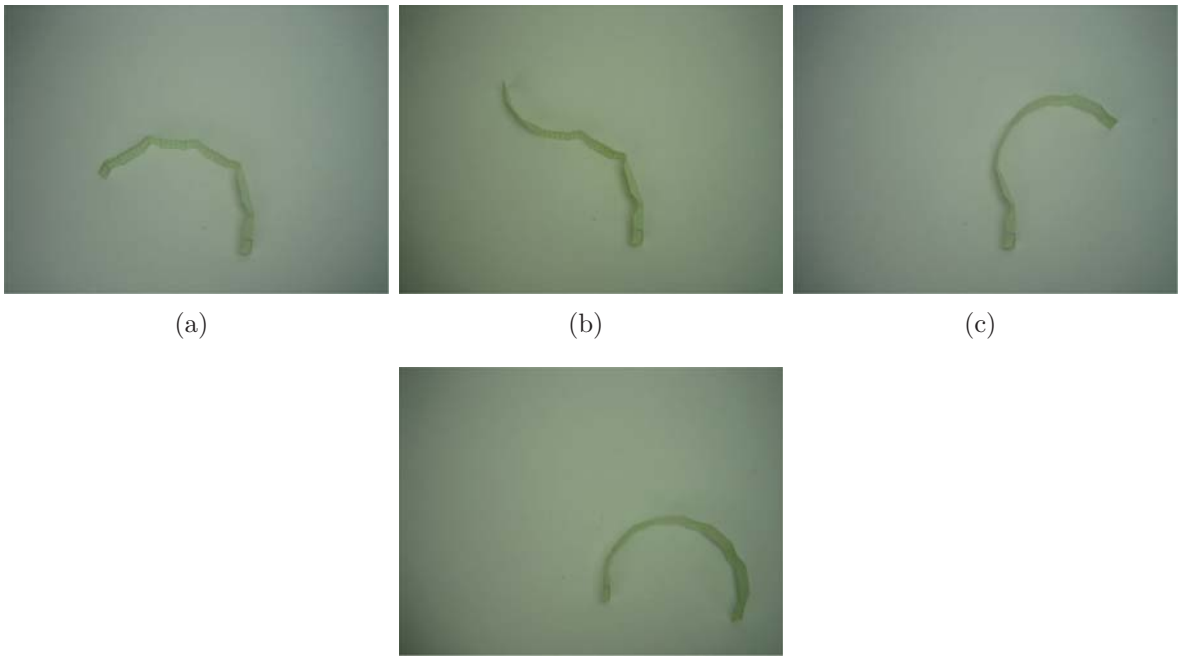

(a) (b) (c)

(d)

Figure 3.18: Digital origami strip as it transforms from (a) state with all WBs in "off" position through (b), (c) intermediate states to (d) state with all WBs in "on" position. Because the "on" and "off" states are non-identical, the global curvatures in (a) and (d) are different.

compressive force applied in the closed position could be tuned by adjusting the location of the closed state relative to the open one. Figure 3.20 is an example of an n=4 SFWB grasper designed to grip a sphere.

3.6 Conclusion

Models have been developed to describe the behavior of the generalized waterbomb base (WB), including the kinematic, potential energy, and force-deflection analyses. The relative effect that the number of folds has on the behavior was analyzed, including the effect on dihedral angles, potential energy curves, and actuation force. The bistable split-fold waterbomb base was introduced, with its corresponding analyses, including the effect that the split-fold panel size has on device behavior (e.g. dihedral angles, potential energy, and actuation force). Potential energy analyses were completed to predict the bistable behavior

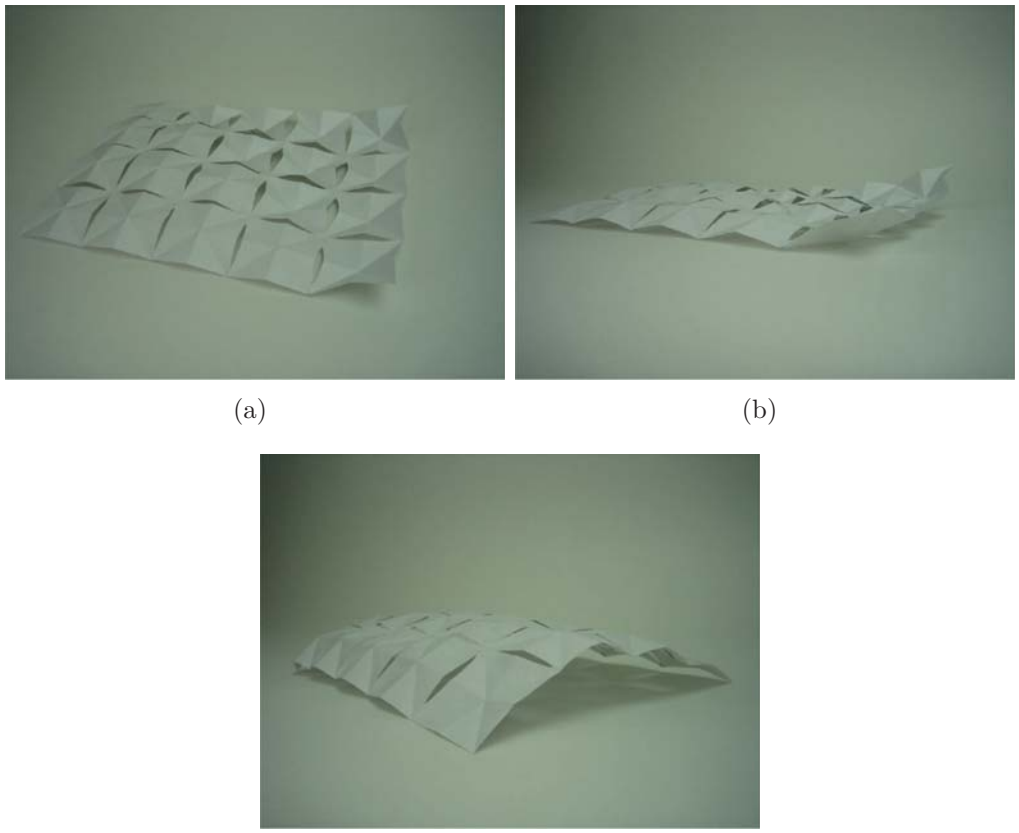

(a) (b)

(c)

Figure 3.19: (a) A 4-unit by 5-unit digital origami sheet in (b) a wave configuration and (c) an arch configuration. By choosing which WB elements are "on" and "off", the global shape of the sheet can be altered dramatically.

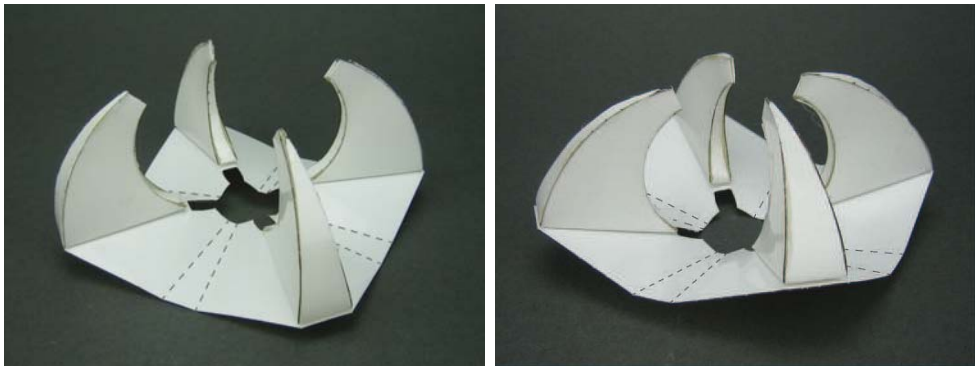

(a) (b)

Figure 3.20: Polycarbonate gripper prototype in the (a) open and (b) closed positions. It was designed to grasp a sphere. Lines are shown on the plastic sheet to identify the crease locations.

of both types of waterbomb base, and the principle of virtual work was used to develop force-deflection predictions.

The WB and SFWB have some behavioral features in common. The stable states of both can be adjusted by changing the k_{γ_m}:k_{γ_v} ratio so as to make the second stable state either a "cocked" position or something closer in energy level to the first stable state. Also, the lower the degree of the mechanism, the easier it is to achieve the cocked position. When k_{γ_m}=k_{γ_v}, the magnitude of k does not affect where the stable states occur, but only the magnitudes of the potential energy and acutation forces.

A few functional differences also exist. Lower force and potential energy values are involved in the SFWBs when compared to their equivalent-degree WBs. The extra links present in the SFWBs present opportunities for greater customizability than what is present in the WB.

CHAPTER 4. CONCLUSIONS AND RECOMMENDATIONS

This thesis presents models for the kinetic behavior of the traditional origami waterbomb base as well as two of its generalized forms - the generalized waterbomb base (WB) and the generalized split-fold waterbomb base (SFWB). Models of the kinematic and bistable behaviors (including force-deflection behavior) of the traditional waterbomb base undergoing symmetric motion were validated through comparison to 3-D CAD models, physical prototype testing, and finite element analysis. These models were then extended to degree n rotationally symmetric, developable generalized WBs and SFWBs also undergoing rotationally symmetric motion. Using these models, the positions and locations of bistable states, as well as the forces required to move between them, can be predicted and tuned to suit different situations and needs.

These models are meant to facilitate the development of this common origami fold into useful mechanisms and other applications. Possible applications such as simple springs or switches as well as more complicated devices such as customizable grippers or testbeds for actuation are briefly discussed, but the geometric and behavioral modifiability of these waterbomb bases could be attractive in a much broader range of uses. It is hoped that for many of these applications, the models presented here will provide a valuable first step from which designers can move toward a more complete design.

4.1 Recommendations for future work

Future work could be focused on designing novel mechanisms or integrating a WB into an existing mechanism or design using these models. Subsequent studies could also investigate waterbomb bases that are not so rigidly constrained as those considered here. Non-developable (sum of all sector angles $\neq 360°$) and non-symmetric geometries would require more complex models but would undoubtedly exhibit their own interesting behaviors.

Symmetric configurations and motions are often empirically observed and will operate at the lowest energy levels in many cases, but there may be instances in which non-symmetric motion between stable states could be energetically preferential. This spontaneous symmetry breaking, or buckling, would be an interesting topic for future investigation.

REFERENCES

[1] Balkcom, D. J., and Mason, M. T., 2008. "Robotic origami folding." *The International Journal of Robotics Research,* **27**, pp. 613–627. 1, 7

[2] Dai, J. S., and Jones, J. R., 2002. "Kinematics and mobility analysis of carton folds in packing manipulation based on the mechanism equivalent." *Proceedings of the Institution of Mechanical Engineers, Part C: Journal of Mechanical Engineering Science,* **216**, pp. 959–970. 1, 7, 29

[3] Crömvik, C., 2007. "Numerical folding of airbags based on optimization and origami." PhD thesis, Chalmers University of Technology and Goteborg University. 1, 7

[4] Tachi, T., 2006. "Simulation of rigid origami." In *Origami 4: Fourth International Meeting of Origami Science, Mathematics, and Education.* 1, 7, 29

[5] Mentrasti, L., Cannella, F., Pupilli, M., and Dai, J. S., 2013. "Large bending behavior of creased paperboard. I. experimental investigations." *International Journal of Solids and Structures,* **50**, pp. 3089–3096. 1, 7, 30

[6] Nagasawa, S., Fukuzawa, Y., Yamaguchi, T., Tsukatani, S., and Katayama, I., 2003. "Effect of crease depth and crease deviation on folding deformation characteristics of coated paperboard." *Journal of Materials Processing Technology,* **140**, pp. 157–162. 1, 7, 30

[7] Francis, K. C., Blanch, J. E., Magleby, S. P., and Howell, L. L., 2013. "Origami-like creases in sheet materials for compliant mechanism design." *Mechanical Sciences,* **4**, pp. 371–380. 1, 7, 30

[8] Howell, L. L., 2001. *Compliant Mechanisms.* John Wiley & Sons, Inc., New York, NY. 1, 7, 9, 14, 23, 30

[9] Greenberg, H. C., Gong, M. L., Magleby, S. P., and Howell, L. L., 2011. "Identifying links between origami and compliant mechanisms." *Mechanical Sciences,* **2**, pp. 217–225 Mechanical Sciences is a special issue associated with the Second International Symposium on Compliant Mechanisms, Delft, The Netherlands. 1, 7, 30

[10] Willis, A. M., 2012. Collapsible kayak, U.S. patent 8316788B2. 1, 7

[11] Fite, F. B., Ming, N. H., and Ho, T. L., 2008. Foldable plastic bowl, U.S. patent D567592. 1, 7

[12] Heller, A., 2003. "A giant leap for space telescopes." *Science & Technology Review,* **March**, pp. 12–18. 1, 7

[13] Zirbel, S. A., Lang, R. J., Magleby, S. P., Thomson, M. W., Sigel, D. A., Walkemeyer, P. E., Trease, B. P., and Howell, L. L., 2013. "Accommodating thickness in origami-based deployable arrays." *Journal of Mechanical Design,* **135**, p. 111005. 1, 7, 29

[14] Ma, J., and You, Z., 2013. "A novel origami crash box with varying profiles." In *Proceedings of the ASME 2013 International Design Engineering Technical Conferences.* 1

[15] Martinez, R. V., Fish, C. R., Chen, X., and Whitesides, G. M., 2012. "Elastomeric origami: Programmable paper-elastomer composites as pneumatic actuators." *Advanced Functional Materials,* **22**, pp. 1376–1384. 1, 7, 29

[16] Felton, S., Tolley, M., Demaine, E., Rus, D., and Wood, R., 2014. "A method for self-folding machines." *Science,* **345**(6197), August, pp. 644–646. 1, 29

[17] Silverberg, J. L., Evans, A. A., McLeod, L., Hayward, R. C., Hull, T., Santangelo, C. D., and Cohen, I., 2014. "Using origami design principles to fold reprogrammable mechanical metamaterials." *Science,* **345**(6197), August, pp. 647–650. 1, 27

[18] Randlett, S., 1963. *The Art of Origami.* Faber and Faber. 2, 27

[19] Giegher, M., 1639. *Le Trie Trattati.* Paolo Frambotto. 2, 27

[20] Bowen, L. A., Frecker, M., Simpson, T. W., and von Lockette, P., 2014. "A dynamic model of magneto-active elastomer actuation of the waterbomb base." *Proceedings of the ASME 2014 International Design Engineering Technical Conference.* 2

[21] Lang, R. J., 2011. *Origami Design Secrets: Mathematical Methods for an Ancient Art.* A K Peters/CRC Press. 5, 10, 27, 31

[22] Guo, W., Li, M., and Zhou, J., 2013. "Modeling programmable deformation of self–folding all–polymer structures with temperature–sensitive hydrogels." *Smart Materials and Structures,* **22**. 5, 49

[23] Liu, Y., Boyles, J. K., Genzer, J., and Dickey, M. D., 2012. "Self-folding of polymer sheets using local light absorption." *The Royal Society of Chemistry,* **Soft Matter (8)**, pp. 1764–1769. 5, 49

[24] Ahmed, S., Lauff, C., Crivaro, A., McGough, K., Sheridan, R., Frecker, M., von Lockette, P., Ounaies, Z., Simpson, T., Lien, J.-M., and Strzelec, R., 2013. "Multi-field responsive origami structures: Preliminary modeling and experiments." In *Proceedings of the ASME 2013 International Design Engineering Technical Conferences and Computers and Information in Engineering Conference, paper no. DETC2013–12405.* 5, 49

[25] Sterman, Y., Demaine, E. D., and Oxman, N., 2013. "PCB origami: A material-based design approach to computer-aided foldable electronic devices." *Journal of Mechanical Design,* **135**(11), October, p. 114502. 5, 49

[26] Ma, J., and You, Z., 2011. "The origami crash box." In *Origami 5: Fifth International Meeting of Origami Science, Mathematics, and Education.* 7

[27] Dai, J. S., and Cannella, F., 2008. "Stiffness characteristics of carton folds for packaging." *Journal of Mechanical Design,* **130**, p. 022305. 7, 30

[28] Nagasawa, S., M., M. N. B., and Shiga, Y., 2011. "Bending moment characteristics on repeated folding motion of coated paperboard scored by round-edge knife." *Journal of Advanced Mechanical Design, Systems, and Manufacturing,* **5**, pp. 385–394. 7, 30

[29] Jensen, B. D., and Howell, L. L., 2004. "Bistable configurations of compliant mechanisms modeled using four links and translational joints." *Journal of Mechanical Design,* **126**(4), pp. 657–666. 8, 30

[30] Pucheta, M. A., and Cardona, A., 2010. "Design of bistable compliant mechanisms using precision-position and rigid-body replacement methods." *Mechanism and Machine Theory,* **45**, pp. 304–326. 8, 30

[31] Ishii, H., and Ting, K.-L., 2004. "SMA actuated compliant bistable mechanisms." *Mechatronics,* **14**, pp. 421–437. 8, 30

[32] Wilcox, D. L., and Howell, L. L., 2005. "Fully compliant tensural bistable micromechanisms (FTBM)." *Journal of Microelectromechanical Systems,* **14**(6), pp. 1223–1235. 8, 30

[33] Smith, C. L., and Lusk, C. P., 2011. "Modeling and parameter study of bistable spherical compliant mechanisms." In *ASME 2011 International Design Engineering Technical Conferences and Computers and Information in Engineering Conference*. 10

[34] Lusk, C. P., and Howell, L. L., 2008. "Spherical bistable micromechanism." *ASME Journal of Mechanical Design,* **130**(4), pp. 045001–6 to 045001–6. 10

[35] Chiang, C. H., 2009. *Kinematics of Spherical Mechanisms*. Krieger Publishing Company. 13, 29, 32

[36] Homer, E. R., Harris, M. B., Zirbel, S. A., Kolodziejska, J. A., Kozachkov, H., Trease, B. P., Borgonia, J.-P. C., Agnes, G. S., Howell, L. L., and Hofmann, D. C., 2014. "New methods for developing and manufacturing compliant mechanisms utilizing bulk metallic glass." *Advanced Engineering Materials,* **16**(7), July, pp. 850–856. 17, 50

[37] Hanna, B. H., Lund, J. M., Lang, R. J., Magleby, S. P., and Howell, L. L., 2014. "Waterbomb base: a symmetric single-vertex bistable origami mechanism." *Smart Materials and Structures,* **23**, p. 094009. 27, 30, 34, 36, 38, 48, 49

[38] Tachi, T., 2013. "Designing freeform origami tessellations by generalizing Resch's patterns." *Journal of Mechanical Design,* **135**, p. 111006. 27, 31

[39] Miura, K., 1985. "Method of packaging and deployment of large membranes in space." *Intstitute of Space and Astronautical Science,* **618**, pp. 1 – 9. 27

[40] Schenk, M., and Guest, S. D., 2012. "Geometry of muira-folded metamaterials." *Proceedings of the National Academy of Sciences of the United States of America,* **110**(9), pp. 3276 – 3281. 27

[41] Mahadevan, L., and Rica, S., 2005. "Self-organized origami." *Science,* **307**(5716), p. 1740. 29

[42] Ma, J., and You, Z., 2013. "Energy absorption of thin-walled square tubes with a prefolded origami pattern – part I: Geometry and numerical simulation." *Journal of Applied Mechanics,* **81(1)**, p. 011003. 29

[43] Guest, S. D., and Pellegrino, S., 1994. "The folding of triangulated cylinders, part I: Geometric considerations." *Journal of Applied Mechanics,* **61(4)**, pp. 773–777. 29

[44] Guest, S. D., and Pellegrino, S., 1994. "The folding of triangulated cylinders, part II: The folding process." *Journal of Applied Mechanics,* **61(4)**, pp. 778–783. 29

[45] Guest, S. D., and Pellegrino, S., 1996. "The folding of triangulated cylinders, part III: Experiments." *Journal of Applied Mechanics,* **63(1)**, pp. 77–83. 29

[46] Hawkes, E., An, B., Benbernou, N. M., Tanaka, H., Kim, S., Demaine, E. D., Rus, D., and Wood, R. J., 2010. "Programmable matter by folding." *Proceedings of the National Academy of Sciences of the United States of America,* **107**, pp. 12441–12445. 29

[47] Tachi, T., 2010. "Geometric considerations for the design of rigid origami structures." In *Proceedings of the International Association for Shell and Spatial Structures (IASS) Symposium 2010*. 29

[48] Winder, B., Magleby, S., and Howell, L., 2009. "Kinematic representations of pop-up paper mechanisms." *Journal of Mechanisms and Robotics,* **1**(2), pp. 021009–1 to 021009–10. 29

[49] Belcastro, S., and Hull, T. C., 2002. "Modelling the folding of paper into three dimensions using affine transformations." *Linear Algebra and its Applications,* **348**, June, pp. 273–282. 29

[50] Bowen, L. A., Grames, C. L., Magleby, S. P., Howell, L. L., and Lang, R. J., 2013. "A classification of action origami as systems of spherical mechanisms." *Journal of Mechanical Design,* **135**(11), October, p. 111008. 29, 32

[51] Beharic, J., Lucas, T. M., and Harnett, C. K., 2014. "Analysis of a compressed bistable buckled beam on a flexible support." *Journal of Applied Mechanics,* **81(8)**, p. 081001. 30

[52] Tanner, J. D., and Jensen, B. D., 2013. "Power-free bistable threshold accelerometer made from a carbon nanotube framework." *Journal of Mechanical Sciences,* **4**, pp. 397–405. 30